CrossMark

J. Fluid Mech. (2016), *vol.* 804, *pp.* 224–247. © Cambridge University Press 2016
doi:10.1017/jfm.2016.533

Elliptic instability of a curved Batchelor vortex

Francisco J. Blanco-Rodríguez[1] **and Stéphane Le Dizès**[1],†

[1]Aix Marseille Univ, CNRS, Centrale Marseille, IRPHE, F-13013 Marseille, France

(Received 22 January 2016; revised 3 May 2016; accepted 12 August 2016;
first published online 9 September 2016)

The occurrence of the elliptic instability in rings and helical vortices is analysed theoretically. The framework developed by Moore & Saffman (*Proc. R. Soc. Lond.* A, vol. 346, 1975, pp. 413–425), where the elliptic instability is interpreted as a resonance of two Kelvin modes with a strained induced correction, is used to obtain the general stability properties of a curved and strained Batchelor vortex. Explicit expressions for the characteristics of the three main unstable modes are obtained as a function of the axial flow parameter of the Batchelor vortex. We show that vortex curvature adds a contribution to the elliptic instability growth rate. The results are applied to a single vortex ring, an array of alternate vortex rings and a double helical vortex.

Key words: vortex flows, vortex instability

1. Introduction

The elliptic instability is a short-wavelength instability developing in the core of strained vortices. Moore & Saffman (1975) showed that this instability can be understood as a mechanism of resonance of two Kelvin modes of the vortex with the elliptic correction induced by an external strain field. In the present work, we use this framework to obtain the characteristics of the elliptic instability for a curved Batchelor vortex.

The elliptic instability is different from the long-wavelength instability observed in vortex pairs (Crow 1970) and helical vortices (Widnall 1972; Okulov 2004; Quaranta, Bolnot & Leweke 2015), and from the swirling-jet instability occurring in a straight Batchelor vortex with large axial flow (Mayer & Powell 1992). It is also different from the so-called curvature instability which involves a different resonance (Fukumoto & Hattori 2005; Hattori & Fukumoto 2014).

The elliptic instability has been observed in numerous contexts (see Kerswell 2002, for a review). It almost systematically appears during vortex interactions (Leweke, Le Dizès & Williamson 2016). Leweke & Williamson (1998) and Meunier & Leweke (2005) provided nice experimental evidence of this instability in straight vortex pairs. It is also expected to be present in vortex rings (Widnall, Bliss & Tsai 1974) and helical vortices (Leweke *et al.* 2014).

Most theoretical works have concerned vortices without axial flow. The first studies considered the Rankine vortex (uniform vorticity in the core) to be able to compute

† Email address for correspondence: ledizes@irphe.univ-mrs.fr

https://doi.org/10.1017/jfm.2016.533 Published online by Cambridge University Press

the Kelvin modes and the elliptic correction explicitly (Tsai & Widnall 1976; Widnall & Tsai 1977; Eloy & Le Dizès 2001; Fukumoto 2003). However, this model gave many resonant configurations with similar growth rates which were never observed in experiments. A better agreement with experiments was obtained using the Lamb–Oseen vortex (Eloy & Le Dizès 1999; Le Dizès & Laporte 2002). For this model, Sipp & Jacquin (2003) demonstrated that numerous resonant modes which were present for the Rankine vortex are not present anymore for a Lamb–Oseen vortex owing to the appearance of a critical layer singularity. The effect of the critical layer was shown to damp the mode and therefore suppress the resonance (Le Dizès 2004; Le Dizès & Lacaze 2005; Fabre, Sipp & Jacquin 2006).

The critical layer damping of the modes also explains the difference between the Rankine vortex and the Lamb–Oseen vortex in the presence of axial flow. Among the numerous modes obtained for the Rankine vortex (Lacaze, Birbaud & Le Dizès 2005), only a few are possible for the Batchelor vortex (Lacaze, Ryan & Le Dizès 2007). For moderate Reynolds number and small strain rate, Lacaze *et al.* (2007) demonstrated that only three different modes could become the most unstable. In the present study, we will focus on these three modes.

In the framework of Moore & Saffman (1975), the characteristics of the elliptic instability mode only depend on the underlying vortex model. Its growth rate, however, depends on the elliptic deformation and, therefore, on the local strain rate felt by the vortex. The elliptic deformation was first described in the context of straight vortices (Ting & Tung 1965; Moffatt, Kida & Ohkitani 1994; Jiménez, Moffatt & Vasco 1996). It depends in a nonlinear way on the vortex profile but remains proportional to the external strain rate. This model was recently extended to general curved vortices by Blanco-Rodriguez *et al.* (2015). They showed that curvature modifies the elliptic correction by adding a contribution dependent of the local curvature of the vortex. Widnall & Tsai (1977) computed this contribution for a Rankine vortex ring. They obtained the only known prediction of the elliptic instability in a curved vortex, but this prediction is limited to a Rankine vortex without axial flow.

In the present work, we extend their analysis to a realistic vortex with axial flow. We provide general formulae which can be used for any values of the axial flow parameter. The results are applied not only to a ring with swirl, but also to ring arrays and multiple helical vortices.

The paper is organized as follows. In §§ 2 and 3, we describe the base flow and provide the perturbation equations. A formal expression of the instability growth rate is derived in § 4. The coefficients of this expression are computed in § 6 for the resonance modes which are characterized in § 5. The effect of curvature is documented in § 7. The results are then applied to particular configurations in § 8. The appendices provide additional details on the base flow, the governing equations and the coefficients of the growth rate expression.

2. Base flow

We are interested in perturbations developing in the core of a moving vortex structure which constitutes our base flow. We assume that there exist a (moving) local frame where the base flow is locally and, to first approximation, a stationary straight axisymmetric vortex with axial flow. This hypothesis implies that the local curvature radius κ of the vortex centreline and the shortest distance δ to other vortex structures are both large compared to the core size a of the vortex. In other words, the vortex structure can be described at leading order as a filament. The weak background

https://doi.org/10.1017/jfm.2016.533 Published online by Cambridge University Press

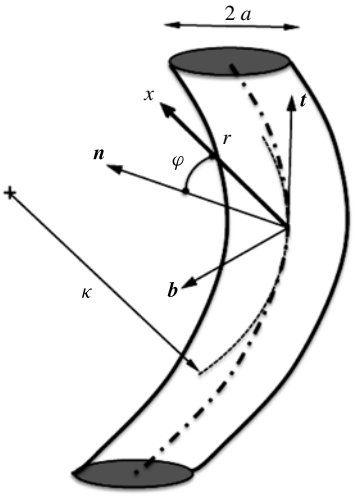


FIGURE 1. Sketch of the local coordinate system in the Frenet frame ($\boldsymbol{t}$, $\boldsymbol{n}$, $\boldsymbol{b}$) of the centreline.

speed associated with the change of frame is also neglected, which is justified for the applications that we consider in § 8 (Blanco-Rodriguez *et al.* 2015).

The vortex core dynamics is analysed using a local 'cylindrical' coordinate system (r, φ, s) constructed from the local Frenet frame ($\boldsymbol{t}$, $\boldsymbol{n}$, $\boldsymbol{b}$) attached to the vortex centreline (see Callegari & Ting 1978), as described in figure 1.

This coordinate system is not orthogonal, but it is related to the orthogonal curvilinear coordinate system (r, θ, s) if $\theta = \varphi + \int^s \tau \, \mathrm{d}s$, τ being the torsion. In this frame, the internal vortex structure can be decomposed into multipolar components $f = f_0(r) + f_1(r)\mathrm{e}^{\mathrm{i}\varphi} + f_2(r)\mathrm{e}^{2\mathrm{i}\varphi} + \cdots$. Moreover, if we assume that κ and δ are of the same order, each multipolar component can be expanded in terms of a single parameter $\varepsilon = a/\kappa$.

The leading-order monopolar component is the prescribed underlying straight vortex of velocity–pressure field $\boldsymbol{U}_m = (0, V^{(0)}(r), W^{(0)}(r), P^{(0)}(r))$. Here, we consider the Batchelor vortex profile defined by

$$V^{(0)} = \frac{1 - \mathrm{e}^{-r^2}}{r}, \tag{2.1a}$$

$$W^{(0)} = W_0 \mathrm{e}^{-r^2}. \tag{2.1b}$$

Spatial and time scales have been non-dimensionalized using the core size a and the maximum angular velocity of the vortex $\Omega^{(0)}_{max} = \Gamma/(2\pi a^2)$, Γ being the vortex circulation. The axial flow parameter W_0 is defined as the ratio

$$W_0 = \frac{W^{(0)}_{max}}{\Omega^{(0)}_{max} a}. \tag{2.2}$$

Here, we assume that $W_0 \leqslant 0.5$ such that the vortex remains unaffected by the inviscid swirling-jet instability (Mayer & Powell 1992).

The dipolar correction is of order ε and is due to local curvature effects only, as was calculated by Callegari & Ting (1978). If the vortex centre is conveniently chosen as

https://doi.org/10.1017/jfm.2016.533 Published online by Cambridge University Press

a stagnation point of the radial and azimuthal velocity components, a parameter-free expression of this correction is obtained as

$$\boldsymbol{U}_d \sim \varepsilon\,\mathrm{Re}(\boldsymbol{U}^{(1)}\mathrm{e}^{\mathrm{i}\varphi}) = \frac{\varepsilon}{2}\begin{pmatrix}\mathrm{i}U^{(1)}(r)\\ V^{(1)}(r)\\ W^{(1)}(r)\\ P^{(1)}(r)\end{pmatrix}\mathrm{e}^{\mathrm{i}\varphi} + \text{c.c.}, \tag{2.3}$$

where expressions for $U^{(1)}$, $V^{(1)}$, $W^{(1)}$, $P^{(1)}$ are provided in appendix A.

The quadripolar correction responsible for the elliptic instability appears at second order in ε. As shown in Blanco-Rodriguez *et al.* (2015), this correction can be divided into two parts

$$\boldsymbol{U}_q \sim \varepsilon^2\,\mathrm{Re}((S\boldsymbol{U}^{(2)} + \boldsymbol{U}_\varepsilon^{(2)})\mathrm{e}^{2\mathrm{i}\varphi}) = \frac{\varepsilon^2}{2}\left\{S\begin{pmatrix}\mathrm{i}U^{(2)}(r)\\ V^{(2)}(r)\\ W^{(2)}(r)\\ P^{(2)}(r)\end{pmatrix} + \begin{pmatrix}\mathrm{i}U_\varepsilon^{(2)}(r)\\ V_\varepsilon^{(2)}(r)\\ W_\varepsilon^{(2)}(r)\\ P_\varepsilon^{(2)}(r)\end{pmatrix}\right\}\mathrm{e}^{2\mathrm{i}\varphi} + \text{c.c.}, \tag{2.4}$$

where $\boldsymbol{U}^{(2)}$ and $\boldsymbol{U}_\varepsilon^{(2)}$ are also provided in appendix A. The second term is a local term generated by curvature. The first term is a strain field contribution: its velocity field reduces to a pure strain field of strain rate $S_{ext} = 2\varepsilon^2 S$ as $r \to \infty$. As explained in Blanco-Rodriguez *et al.* (2015), the parameter S is the only term which changes from one configuration to another. As we shall see in § 8, it can vanish for helices or vortex ring arrays.

3. Perturbation equations

The dimensionless form of the Euler equations in the orthogonal curvilinear coordinate system (r, θ, s) reads (see Callegari & Ting 1978)

$$U_t + UU_r + \frac{V}{r}(U_\theta - V) + \frac{WU_s}{h} + P_r + \frac{\varepsilon}{h}W^2\cos\varphi = 0, \tag{3.1a}$$

$$V_t + UV_r + \frac{V}{r}(V_\theta + U) + \frac{WV_s}{h} + \frac{P_\theta}{r} - \frac{\varepsilon}{h}W^2\sin\varphi = 0, \tag{3.1b}$$

$$W_t + UW_r + \frac{V}{r}W_\theta + \frac{WW_s}{h} + \frac{P_s}{h} - \frac{\varepsilon}{h}(U\cos\varphi - V\sin\varphi)W = 0, \tag{3.1c}$$

$$\frac{1}{r}(rU)_r + \frac{V_\theta}{r} + \frac{W_s}{h} + \frac{\varepsilon}{h}(U\cos\varphi - V\sin\varphi) = 0, \tag{3.1d}$$

where $h = 1 - \varepsilon r\cos\varphi$, $\varphi = \theta - \alpha\varepsilon s$ and $\alpha = \tau/\kappa$.

The perturbation equations are obtained by linearizing the Euler equations around the base flow $\boldsymbol{U} \sim \boldsymbol{U}^{(0)} + \mathrm{Re}(\varepsilon\boldsymbol{U}^{(1)}\mathrm{e}^{\mathrm{i}\varphi} + \varepsilon^2(S\boldsymbol{U}^{(2)} + \boldsymbol{U}_\varepsilon^{(2)})\mathrm{e}^{2\mathrm{i}\varphi})$. One should note that we do not consider the monopolar and dipolar corrections to the base flow of the order ε^2 as they do not contribute to the elliptic instability. After linearizing, we obtain for the velocity–pressure field $\boldsymbol{u} = (-\mathrm{i}u, v, w, p)$ of the perturbation, a system of the form:

$$\begin{aligned}(\mathrm{i}\partial_t\boldsymbol{I} + \mathrm{i}\partial_s\boldsymbol{P} + \boldsymbol{M})\boldsymbol{u} \;=\; &\varepsilon(\mathrm{e}^{\mathrm{i}\varphi}\boldsymbol{N}_+^{(1)} + \mathrm{e}^{-\mathrm{i}\varphi}\boldsymbol{N}_-^{(1)})\boldsymbol{u} + \varepsilon^2\boldsymbol{D}\boldsymbol{u}\\ &+ \varepsilon^2(\mathrm{e}^{2\mathrm{i}\varphi}(S\boldsymbol{N}_+^{(2)} + \boldsymbol{N}_{\varepsilon+}^{(2)}) + \mathrm{e}^{-2\mathrm{i}\varphi}(S\boldsymbol{N}_-^{(2)} + \boldsymbol{N}_{\varepsilon-}^{(2)}))\boldsymbol{u},\end{aligned} \tag{3.2}$$

where the operators $\boldsymbol{I}$, $\boldsymbol{P}$, $\boldsymbol{M} = \boldsymbol{M}(-\mathrm{i}\partial_\varphi)$, $\boldsymbol{D} = \boldsymbol{D}(-\mathrm{i}\partial_s)$, $\boldsymbol{N}_\pm^{(1)} = \boldsymbol{N}_\pm^{(1)}(-\mathrm{i}\partial_\varphi, -\mathrm{i}\partial_s)$, $\boldsymbol{N}_\pm^{(2)} = \boldsymbol{N}_\pm^{(2)}(-\mathrm{i}\partial_\varphi, -\mathrm{i}\partial_s)$ and $\boldsymbol{N}_{\varepsilon\pm}^{(2)} = \boldsymbol{N}_{\varepsilon\pm}^{(2)}(-\mathrm{i}\partial_\varphi, -\mathrm{i}\partial_s)$ are defined in appendix B.

https://doi.org/10.1017/jfm.2016.533 Published online by Cambridge University Press

The left-hand side corresponds to the inviscid perturbation equations of the undeformed Batchelor vortex. The dipolar term (first term) on the right-hand side is responsible for the curvature instability while the quadripolar term (third term) is responsible for the elliptic instability. Note that the perturbation equations for a straight vortex in a strain field (of strain rate S_{ext}) are obtained from (3.2) by setting $\varepsilon \to 0$ while keeping $2\varepsilon^2 S = S_{ext}$ constant.

In this work, we shall also consider weak viscous effects on the perturbations which amount to add a fourth term on the right-hand side of the form

$$\frac{\mathrm{i}}{Re}\boldsymbol{V}(-\mathrm{i}\partial_\varphi, -\mathrm{i}\partial_s)\boldsymbol{u}, \tag{3.3}$$

where $\boldsymbol{V}(-\mathrm{i}\partial_\varphi, -\mathrm{i}\partial_s)$ is given by (B 3), and the Reynolds number, Re, by

$$Re = \frac{\Omega^{(0)}_{max} a^2}{\nu} = \frac{\Gamma}{2\pi\nu}, \tag{3.4}$$

with ν the kinematic viscosity.

4. Growth rate expression for the elliptic instability

As explained by Moore & Saffman (1975), the elliptic instability results from the resonant coupling of two Kelvin modes of the undeformed vortex with the quadripolar (elliptic) correction to the vortex. Kelvin modes are normal mode solutions of the left-hand side of (3.2). If they are written as

$$\boldsymbol{u} = \tilde{\boldsymbol{u}}(r)\mathrm{e}^{\mathrm{i}ks+\mathrm{i}m\varphi-\mathrm{i}\omega t}, \tag{4.1}$$

$\tilde{\boldsymbol{u}}$ satisfies

$$(\omega\boldsymbol{I} - k\boldsymbol{P} + \boldsymbol{M}(m))\tilde{\boldsymbol{u}} = 0. \tag{4.2}$$

In the following, we shall assume that each Kelvin mode is normalized such that its pressure amplitude $\tilde{p}$ satisfies

$$\tilde{p} \underset{r\to 0}{\sim} r^{|m|}. \tag{4.3}$$

Two Kelvin modes of characteristics (ω_A, k_A, m_A) and (ω_B, k_B, m_B) are resonantly coupled via the quadripolar correction if they satisfy the condition of resonance (assuming $m_A < m_B$)

$$\omega_A = \omega_B, \quad k_A = k_B, \quad m_A = m_B - 2. \tag{4.4a–c}$$

The coupling leads to a growth of the Kelvin mode combination with a maximum growth rate scaling as ε^2. Fukumoto (2003) actually explained that for instability there is an additional condition on the energy of the waves which must be opposite or null. For each resonant configuration, a growth rate expression can be obtained from an orthogonality condition using a classical multiple-scale analysis. Details of the method can be found for instance in Eloy & Le Dizès (1999). The analysis is more complicated in the presence of curvature because additional terms come from a double interaction with the dipolar field. At order ε, each Kelvin mode creates contributions of the same frequency and axial wavenumber but azimuthal wavenumber $m \pm 1$:

$$\boldsymbol{u}^{(1)}_{\pm} = \varepsilon\tilde{\boldsymbol{u}}^{(1)}_{\pm}\mathrm{e}^{\mathrm{i}ks+\mathrm{i}(m\pm1)\varphi-\mathrm{i}\omega t}, \tag{4.5}$$

https://doi.org/10.1017/jfm.2016.533 Published online by Cambridge University Press

where

$$(\omega \boldsymbol{I} - k\boldsymbol{B} + \boldsymbol{M}(m \pm 1))\tilde{\boldsymbol{u}}^{(1)}_{\pm} = \boldsymbol{N}^{(1)}_{\pm}(m, k)\tilde{\boldsymbol{u}}. \tag{4.6}$$

Then, at order ε^2, these contributions generate, by interacting a second time with the dipolar terms, terms of azimuthal wavenumbers m and $m \pm 2$. These last terms are similar to the terms generated by a single interaction of the initial Kelvin mode with the quadripolar terms. They will, then, provide an additional contribution to the coupling terms. The terms of azimuthal wavenumber m are by contrast expected to modify the frequency of the mode.

The final result can be written as an expression for the complex frequency ω of the Kelvin mode combination as a function of the axial wavenumber k:

$$\begin{aligned}&\left(\omega - \omega_c - \mathrm{i}\,\mathrm{Im}\,(\omega_A) - Q_A(k - k_c) - \mathrm{i}\frac{V_A}{Re} - \varepsilon^2 D^{(\varepsilon)}_A\right)\\ &\quad\times\left(\omega - \omega_c - \mathrm{i}\ \mathrm{Im}\,(\omega_B) - Q_B(k - k_c) - \mathrm{i}\frac{V_B}{Re} - \varepsilon^2 D^{(\varepsilon)}_B\right)\\ &= \varepsilon^4 (SR_{AB} + R^{(\varepsilon)}_{AB})(SR_{BA} + R^{(\varepsilon)}_{BA}),\end{aligned} \tag{4.7}$$

where it is implicitly assumed that ω and k are close to the resonant frequency ω_c and wavenumber k_c of the 2 modes. The coefficients of this equation are obtained as scalar products with the adjoint Kelvin modes $\tilde{\boldsymbol{u}}^{\dagger}_A$ and $\tilde{\boldsymbol{u}}^{\dagger}_B$

$$Q_A = \frac{\langle \tilde{\boldsymbol{u}}^{\dagger}_A, \boldsymbol{P}\,\tilde{\boldsymbol{u}}_A\rangle}{\langle \tilde{\boldsymbol{u}}^{\dagger}_A, \boldsymbol{I}\,\tilde{\boldsymbol{u}}_A\rangle}, \quad Q_B = \frac{\langle \tilde{\boldsymbol{u}}^{\dagger}_B, \boldsymbol{P}\,\tilde{\boldsymbol{u}}_B\rangle}{\langle \tilde{\boldsymbol{u}}^{\dagger}_B, \boldsymbol{I}\,\tilde{\boldsymbol{u}}_B\rangle}, \tag{4.8a,b}$$

$$V_A = \frac{\langle \tilde{\boldsymbol{u}}^{\dagger}_A, \boldsymbol{V}\,\tilde{\boldsymbol{u}}_A\rangle}{\langle \tilde{\boldsymbol{u}}^{\dagger}_A, \boldsymbol{I}\,\tilde{\boldsymbol{u}}_A\rangle}, \quad V_B = \frac{\langle \tilde{\boldsymbol{u}}^{\dagger}_B, \boldsymbol{V}\,\tilde{\boldsymbol{u}}_B\rangle}{\langle \tilde{\boldsymbol{u}}^{\dagger}_B, \boldsymbol{I}\,\tilde{\boldsymbol{u}}_B\rangle}, \tag{4.8c,d}$$

$$R_{AB} = \frac{\langle \tilde{\boldsymbol{u}}^{\dagger}_A, \boldsymbol{N}^{(2)}_{+}(m_B, k_B)\,\tilde{\boldsymbol{u}}_B\rangle}{\langle \tilde{\boldsymbol{u}}^{\dagger}_A, \boldsymbol{I}\,\tilde{\boldsymbol{u}}_A\rangle}, \quad R_{BA} = \frac{\langle \tilde{\boldsymbol{u}}^{\dagger}_B, \boldsymbol{N}^{(2)}_{-}(m_A, k_A)\,\tilde{\boldsymbol{u}}_A\rangle}{\langle \tilde{\boldsymbol{u}}^{\dagger}_B, \boldsymbol{I}\,\tilde{\boldsymbol{u}}_B\rangle}, \tag{4.8e,f}$$

$$D^{(\varepsilon)}_A = \frac{\langle \tilde{\boldsymbol{u}}^{\dagger}_A, (\boldsymbol{D}(k_A)\tilde{\boldsymbol{u}}_A + \boldsymbol{N}^{(1)}_{+}(m_A - 1, k_A)\,\tilde{\boldsymbol{u}}^{(1)}_{A-} + \boldsymbol{N}^{(1)}_{-}(m_A + 1, k_A)\,\tilde{\boldsymbol{u}}^{(1)}_{A+})\rangle}{\langle \tilde{\boldsymbol{u}}^{\dagger}_A, \boldsymbol{I}\,\tilde{\boldsymbol{u}}_A\rangle}, \tag{4.9a}$$

$$D^{(\varepsilon)}_B = \frac{\langle \tilde{\boldsymbol{u}}^{\dagger}_B, (\boldsymbol{D}(k_B)\tilde{\boldsymbol{u}}_B + \boldsymbol{N}^{(1)}_{+}(m_B - 1, k_B)\,\tilde{\boldsymbol{u}}^{(1)}_{B-} + \boldsymbol{N}^{(1)}_{-}(m_B + 1, k_B)\,\tilde{\boldsymbol{u}}^{(1)}_{B+})\rangle}{\langle \tilde{\boldsymbol{u}}^{\dagger}_B, \boldsymbol{I}\,\tilde{\boldsymbol{u}}_B\rangle}, \tag{4.9b}$$

$$R^{(\varepsilon)}_{AB} = \frac{\langle \tilde{\boldsymbol{u}}^{\dagger}_A, (\boldsymbol{N}^{(2)}_{\varepsilon-}(m_B, k_B)\,\tilde{\boldsymbol{u}}_B + \boldsymbol{N}^{(1)}_{-}(m_B - 1, k_B)\,\tilde{\boldsymbol{u}}^{(1)}_{B-})\rangle}{\langle \tilde{\boldsymbol{u}}^{\dagger}_A, \boldsymbol{I}\,\tilde{\boldsymbol{u}}_A\rangle}, \tag{4.9c}$$

$$R^{(\varepsilon)}_{BA} = \frac{\langle \tilde{\boldsymbol{u}}^{\dagger}_B, (\boldsymbol{N}^{(2)}_{\varepsilon+}(m_A, k_A)\,\tilde{\boldsymbol{u}}_A + \boldsymbol{N}^{(1)}_{+}(m_A + 1, k_A)\,\tilde{\boldsymbol{u}}^{(1)}_{A+})\rangle}{\langle \tilde{\boldsymbol{u}}^{\dagger}_B, \boldsymbol{I}\,\tilde{\boldsymbol{u}}_B\rangle}, \tag{4.9d}$$

where the adjoint Kelvin modes are defined as solutions to the adjoint equation of (4.2) for the scalar product

$$\langle \boldsymbol{u}_1, \boldsymbol{u}_2\rangle = \int_0^{\infty} \boldsymbol{u}_1^{\star} \cdot \boldsymbol{u}_2 r\,\mathrm{d}r = \int_0^{\infty} (u_1^{\star}u_2 + v_1^{\star}v_2 + w_1^{\star}w_2 + p_1^{\star}p_2) r\,\mathrm{d}r. \tag{4.10}$$

The right-hand side of (4.7) represents the coupling terms. Those proportional to S are associated with the strain field while the others correspond to the additional

https://doi.org/10.1017/jfm.2016.533 Published online by Cambridge University Press

contributions due to the local curvature. The left-hand side of (4.7) gives the dispersion relation of each Kelvin mode close to the resonant point. The terms proportional to ε^2 are correction terms induced by curvature. They are not present in a straight vortex configuration. Note also the presence of the terms $\mathrm{iIm}(\omega_A)$ and $\mathrm{iIm}(\omega_B)$ in the brackets on the left-hand side. These terms have been added to take into account a weak inviscid damping of the modes A and B at the resonant point, associated with the presence of a critical layer singularity (Le Dizès 2004). As we shall see below, only one of the two modes exhibits such a damping.

It is worth mentioning that the coefficients R_{AB}, R_{BA}, $R_{AB}^{(\varepsilon)}$ and $R_{BA}^{(\varepsilon)}$ depend on the normalization of the Kelvin modes. However, equation (4.7) does not, which means that the product on the right-hand side, as well as all the coefficients on the left-hand side, are independent of the Kelvin mode normalization.

The relative amplitude and phase of the resonant Kelvin modes are also provided by the coefficients of (4.7). If the resonant configuration is written as

$$\boldsymbol{u} = a_A \tilde{u}_A \mathrm{e}^{\mathrm{i}ks+\mathrm{i}m_A\varphi-\mathrm{i}\omega t} + a_B \tilde{u}_B \mathrm{e}^{\mathrm{i}ks+\mathrm{i}m_B\varphi-\mathrm{i}\omega t}, \tag{4.11}$$

where a_A and a_B are the complex amplitudes of the two Kelvin modes A and B normalized by (4.3), we obtain an amplitude ratio

$$K_{BA} = \frac{a_B}{a_A} = \frac{\omega - \omega_c - \mathrm{i}\,\mathrm{Im}\,(\omega_A) - Q_A(k-k_c) - \mathrm{i}\dfrac{V_A}{Re} - \varepsilon^2 D_A^{(\varepsilon)}}{\varepsilon^2(SR_{AB} + R_{AB}^{(\varepsilon)})}. \tag{4.12}$$

5. Resonant Kelvin mode characteristics

The conditions of resonance are not affected by curvature effects at leading order, so the characteristics of the resonant Kelvin modes are the same as for straight configurations. For a Batchelor vortex, these characteristics have already been obtained by Lacaze *et al.* (2007).

For each value of m and k, there exists a discrete number of Kelvin modes, which are identified by a third label n, characterizing their radial complexity (typically, the number of radial oscillation in the vortex core). For a Rankine vortex (with or without axial flow), these modes are neutral with frequencies in the interval $[(m-2)+kW_0, (m+2)+kW_0]$. For a smooth vortex profile, such as that of the Batchelor vortex, some of the modes become damped owing to the presence of a critical point singularity (point r_c where $\omega - m\Omega^{(0)}(r_c) - kW^{(0)}(r_c) = 0$) in their radial structure (Le Dizès & Lacaze 2005; Fabre *et al.* 2006). This damping effect becomes strong when the critical point is within the vortex core. This effect introduces a strong difference in the Kelvin mode spectra of Batchelor and Rankine vortices. Numerous resonances which are possible for the Rankine vortex (Lacaze *et al.* 2005) are not present for the Batchelor vortex, because one of the corresponding modes is now strongly damped (Lacaze *et al.* 2007).

Eloy & Le Dizès (2001) and Lacaze *et al.* (2007) also observed that the resonant combinations that are the best coupled (that is, providing the largest growth rates) correspond to branches with the same label n. These resonant combinations, termed 'principal' modes, have been denoted (m_A, m_B, n) where m_A and m_B are the azimuthal numbers of the two resonant Kelvin modes and n their branch label.

For the Batchelor vortex, Lacaze *et al.* (2007) showed that the principal modes $(-1, 1, n)$ progressively disappear as W_0 increases because a critical point in the

https://doi.org/10.1017/jfm.2016.533 Published online by Cambridge University Press

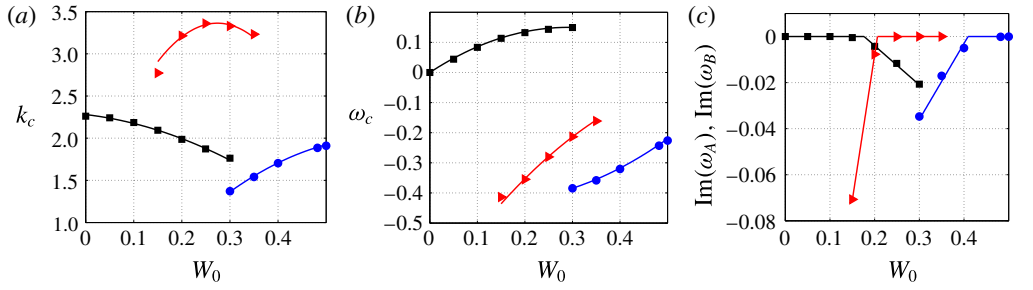


FIGURE 2. (Colour online) Characteristics of the principal modes $(-1, 1, 1)$ (black squares), $(-2, 0, 2)$ (red triangles), $(-2, 0, 1)$ (blue circles) as a function of W_0. (*a*) Axial wavenumber k_c; (*b*) frequency (real part) ω_c; (*c*) critical layer damping $\mathrm{Im}(\omega_A)$ (or $\mathrm{Im}(\omega_B)$) of the resonant Kelvin mode (mode B with $m_B = 1$ for $(-1, 1, 1)$ and mode A with $m_A = -2$ for $(-2, 0, 2)$ and $(-2, 0, 1)$). The solid lines correspond to the fits provided in appendix C.

structure of the Kelvin mode B ($m_B = 1$) appears and moves toward the vortex centre. They also showed that other principal modes, which were not present for $W_0 = 0$, becomes unstable as W_0 increases.

In an inviscid framework, many resonant configurations were found to give a similar growth rate. As soon as viscosity is present, the complicated structures involving large m, k or n are expected to be strongly damped. For moderate Reynolds numbers (say $Re < 10\,000$), Lacaze *et al.* (2007) showed that the stability diagram for $W_0 \leqslant 0.5$ involves only 3 different modes, which are the principal modes $(-1, 1, 1)$, $(-2, 0, 2)$, $(-2, 0, 1)$.

The characteristics of these modes are recalled in figure 2. We have plotted the wavenumber, frequency and critical layer damping of each mode only in the interval where it is expected to exist, that is $0 \leqslant W_0 \leqslant 0.3$ for $(-1, 1, 1)$, $0.15 \leqslant W_0 \leqslant 0.35$ for $(-2, 0, 2)$ and $0.3 \leqslant W_0 \leqslant 0.5$ for $(-2, 0, 1)$. On one side of the interval the mode disappears because one of the two resonant waves becomes too strongly damped. It corresponds to the Kelvin mode B ($m_B = 1$) in $(-1, 1, 1)$ when $W_0 > 0.3$ and to the Kelvin mode A ($m_A = -2$) in $(-2, 0, 2)$ and $(-2, 0, 1)$ when $W_0 < 0.15$ and $W_0 < 0.3$, respectively.

In figure 3, we have displayed the typical spatial structure of the three principal modes for a given set of parameters. We have plotted the vorticity contour of the most unstable principal mode for a particular phase where both Kelvin modes are visible. For each case, we have provided the axial wavenumber, the frequency and the amplitude ratio K_{BA}, defined in (4.12), of the two Kelvin modes that compose the principal mode. Note that the wavenumber and frequency of the principal modes are slightly different from the resonant values k_c and ω_c, which are reported in table 1. This shift depends on the values of ε, S and Re considered.

In figure 3, we can clearly see the azimuthal wavenumbers that compose each principal mode. The branch label parameter is also visible. For both modes $(-1, 1, 1)$ and $(-2, 0, 1)$ there is a single radial oscillation corresponding to the branch label $n = 1$, while in mode $(-2, 0, 2)$, we observe two oscillations as expected for the branch label $n = 2$. The Kelvin mode $m = -2$ of the principal modes $(-2, 0, 1)$ and $(-2, 0, 2)$ possesses a critical point singularity (at $r_c \approx 2.49$ and $r_c \approx 2.36$, respectively) which is sufficiently far away to not affect the spatial structure of the principal mode in the vortex core.

https://doi.org/10.1017/jfm.2016.533 Published online by Cambridge University Press

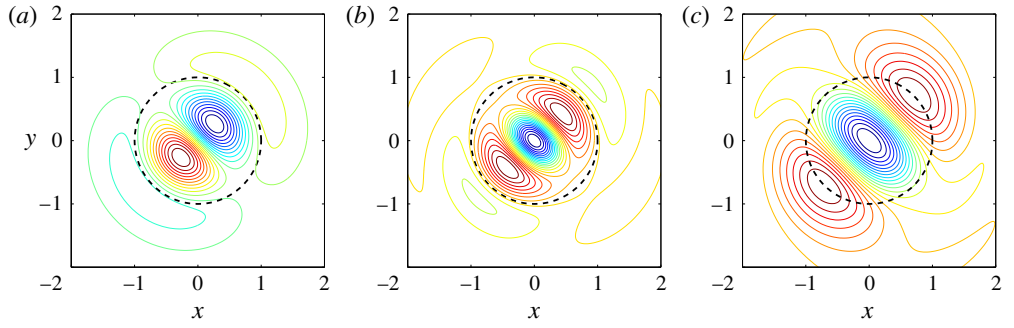


FIGURE 3. (Colour online) Spatial structure of the most dangerous principal modes for typical values of the parameters (here $S = 1$, $\varepsilon^2 = 0.1$, and $Re = 10\,000$). Contours of the axial vorticity of the principal mode in an (x, y) plane defined as $\mathrm{Re}[(\tilde{\zeta}_A(r)\mathrm{e}^{-\mathrm{i}m_A\varphi} + K_{BA}\tilde{\zeta}_B(r)\mathrm{e}^{-\mathrm{i}m_B\varphi})\mathrm{e}^{-\mathrm{i}\pi/2}]$ where $\tilde{\zeta}_A$ and $\tilde{\zeta}_B$ are the axial vorticity amplitude of the Kelvin modes A and B. (a) Mode $(-1, 1, 1)$ for $W_0 = 0$ ($k = 2.2408$, $\omega = 0.1607\mathrm{i}$, $K_{BA} = -0.9994\mathrm{i}$). (b) Mode $(-2, 0, 2)$ for $W_0 = 0.2$ ($k = 3.7742$, $\omega = -0.3759 + 0.1288\mathrm{i}$, $K_{BA} = -0.0258 + 0.3580\mathrm{i}$). (c) Mode $(-2, 0, 1)$ for $W_0 = 0.4$ ($k = 1.9635$, $\omega = -0.3302 + 0.1362\mathrm{i}$, $K_{BA} = -0.0659 + 1.1721\mathrm{i}$).

	$(-1, 1, 1)(W_0 = 0)$	$(-2, 0, 2)(W_0 = 0.2)$	$(-2, 0, 1)(W_0 = 0.4)$
ω_c	0	−0.355	−0.320
k_c	2.261	3.214	1.703
$\mathrm{Im}(\omega_A)$	0	−0.0077	−0.0050
$\mathrm{Im}(\omega_B)$	0	0	0

TABLE 1. Characteristics of the main principal modes.

6. Coefficients of the growth rate formula

In this section we provide the coefficients of the growth rate formula for the resonant configurations giving rise to the principal modes $(-1, 1, 1)$, $(-2, 0, 2)$, $(-2, 0, 1)$.

These coefficients are obtained by computing the integrals defined by (4.8) and (4.9) using the same numerical technique as in Lacaze *et al.* (2007). The results are displayed in figures 4 and 5. For each coefficient, we have also plotted an approximate expression, which is provided in appendix C and which corresponds to a simple polynomial fit of the numerical data. These expressions can be used to obtain the elliptic instability growth rate for any values of W_0, ε, S and Re. It is worth mentioning that the linear coefficients Q_A, Q_B, V_A and V_B are real when there is no critical layer damping. The coefficients Q_A and V_A for $(-1, 1, 1)$ and Q_B and V_B for $(-2, 0, 1)$ and $(-2, 0, 2)$ are therefore always real as they concern the resonant mode with no critical layer ($m_A = -1$ for $(-1, 1, 1)$, $m_B = 0$ for $(-2, 0, 1)$ and $(-2, 0, 2)$). The imaginary parts of the coefficients Q_A and V_A (respectively Q_B and V_B) become non-zero when $\mathrm{Im}(\omega_A)$ (respectively $\mathrm{Im}(\omega_B)$) becomes important. The expression $\mathrm{Im}(\omega_A) + \mathrm{Im}(Q_A)(k - k_c)$ represents an approximation to the critical layer damping of the mode A close to k_c. It is clear that this expression does not apply when it becomes positive. This has to be kept in mind when using (4.7) away from k_c.

https://doi.org/10.1017/jfm.2016.533 Published online by Cambridge University Press

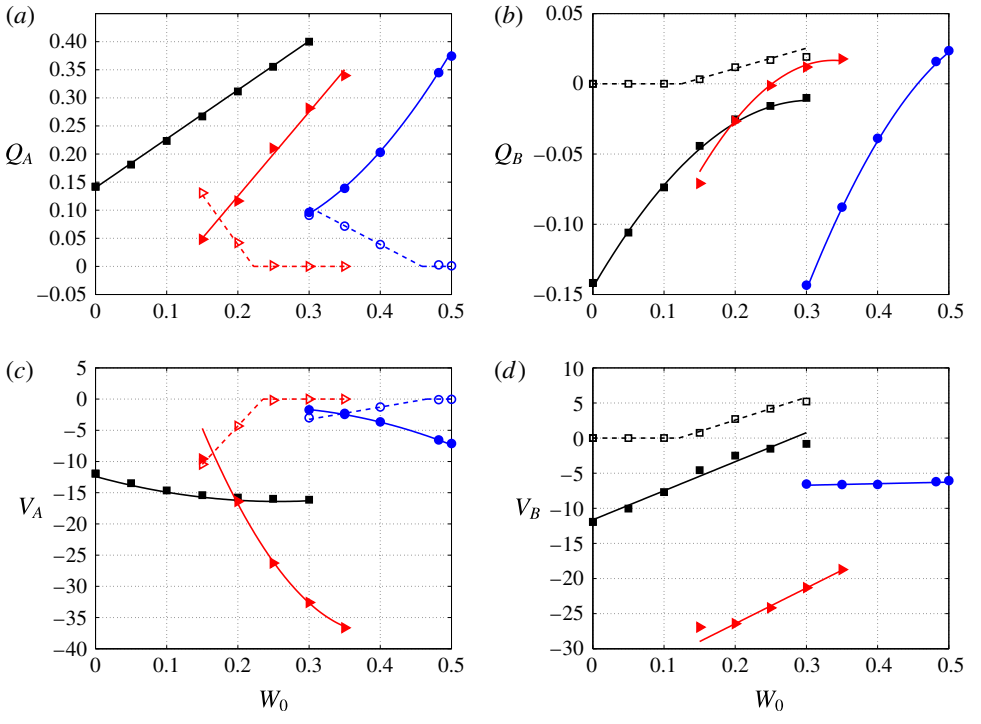


FIGURE 4. (Colour online) Linear coefficients of the growth rate formula for the principal modes $(-1, 1, 1)$ (black squares), $(-2, 0, 2)$ (red triangles), $(-2, 0, 1)$ (blue circles) as a function of W_0. Filled and empty symbols are real part and imaginary part, respectively. The solid and dashed lines are the linear or quadratic fits given in appendix C. (*a*) Q_A, (*b*) Q_B, (*c*) V_A, (*d*) V_B. The coefficients Q_B and V_B (respectively Q_A and V_A) are purely real for the modes $(-2, 0, 2)$ and $(-2, 0, 1)$ (respectively for the mode $(-1, 1, 1)$).

The coefficients $D_A^{(\varepsilon)}$, $D_B^{(\varepsilon)}$, R_{AB}, R_{BA}, $R_{AB}^{(\varepsilon)}$ and $R_{BA}^{(\varepsilon)}$ are coupling coefficients which are generated by interaction with the dipolar and quadripolar corrections to the vortex. The coefficients R_{AB}, R_{BA} are only due to interaction with the strain part of the quadripolar correction. They are the same as those in a straight vortex configuration and were computed in Lacaze *et al.* (2007). The other coupling coefficients are all associated with curvature effects. Note in particular they contain a contribution coming from an interaction with the curvature correction $\boldsymbol{u}_{\pm}^{(1)}$ of each mode (see expressions (4.9*a–d*)). This function has an intricate structure which may involve one or two critical points. Consequently, the coupling coefficients $D_A^{(\varepsilon)}$, $D_B^{(\varepsilon)}$, $R_{AB}^{(\varepsilon)}$ and $R_{BA}^{(\varepsilon)}$ are in general complex even when there is no critical layer damping on the mode itself. Note in particular that the imaginary part of $D_A^{(\varepsilon)}$ and $D_B^{(\varepsilon)}$ can be positive, which means that curvature effects on a single Kelvin mode can become destabilizing. This effect is weak but it implies that resonance is *a priori* not necessary for instability. This surprising result would clearly deserve further studies.

In the following, we shall focus on the three modes $(-1, 1, 1)$, $(-2, 0, 2)$ and $(-2, 0, 1)$ for the particular values $W_0 = 0$, 0.2 and 0.4, respectively. The spatial structures of these modes, as well as their frequencies and wavenumbers, have been provided in figure 3 and table 1. The other coefficients of the growth rate equation are given in table 2.

https://doi.org/10.1017/jfm.2016.533 Published online by Cambridge University Press

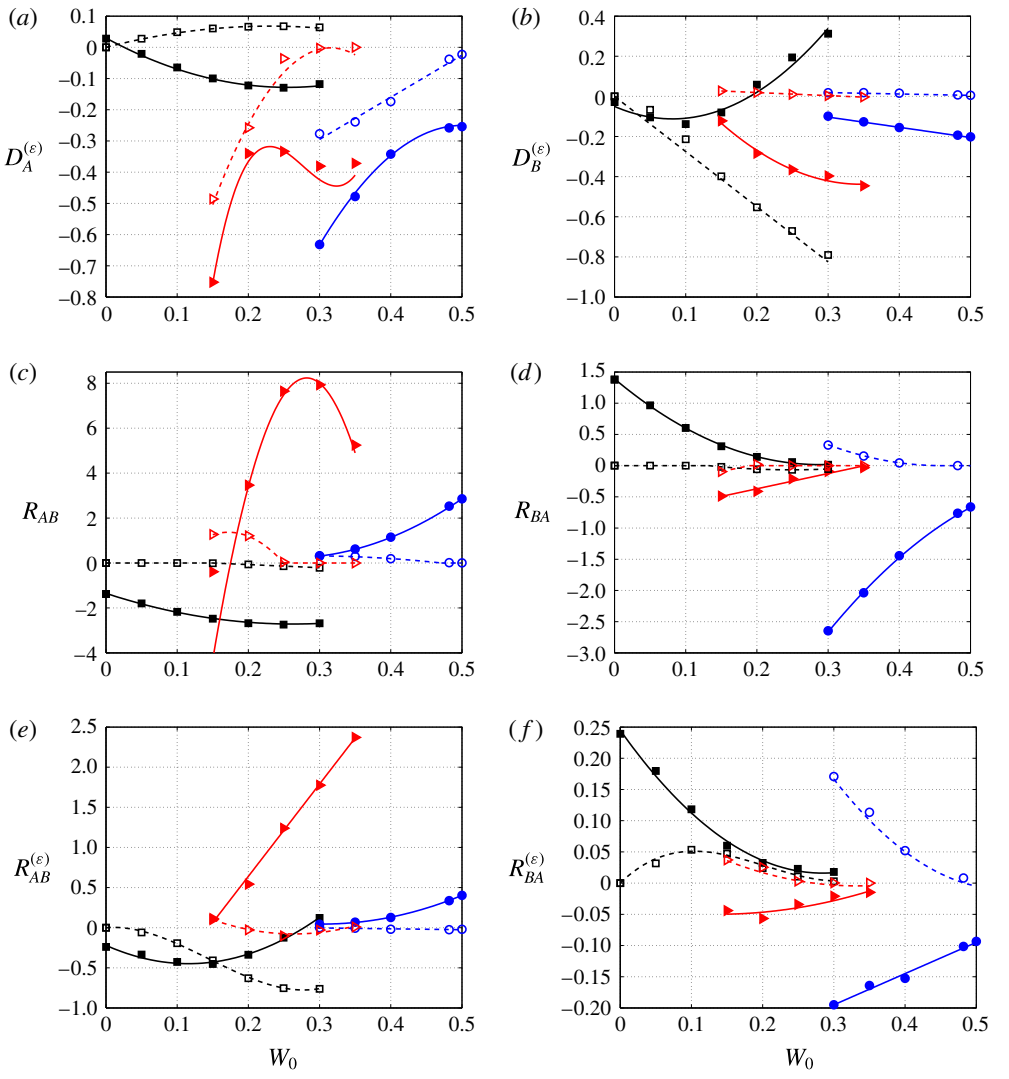


FIGURE 5. (Colour online) Coupling coefficients of the growth rate formula for the principal modes $(-1, 1, 1)$ (black squares), $(-2, 0, 2)$ (red triangles), $(-2, 0, 1)$ (blue circles) as a function of W_0. Filled and empty symbols are real part and imaginary part, respectively. The solid and dashed lines are the polynomial fits given in appendix C. (*a*) $D_A^{(\varepsilon)}$, (*b*) $D_B^{(\varepsilon)}$, (*c*) R_{AB}, (*d*) R_{BA}, (*e*) $R_{AB}^{(\varepsilon)}$, (*f*) $R_{BA}^{(\varepsilon)}$.

7. Curvature effect

In figure 6, we display the contour levels of the maximum growth rate $\sigma_{max}/\varepsilon^2$ for the three modes $(-1, 1, 1)$, $(-2, 0, 2)$ and $(-2, 0, 1)$ at the values $W_0 = 0$, 0.2 and 0.4, respectively. Figure 6(*a–c*) is for an infinite Reynolds number, while (*d–f*) is for $Re = 5000$. Note the qualitative difference between figure 6(*a*) and the other panels. The maximum inviscid growth $\sigma_{max}/\varepsilon^2$ of the mode $(-1, 1, 1)$ for $W_0 = 0$ is found not to depend on ε. For the other modes, $\sigma_{max}/\varepsilon^2$ depends on ε; this is due to the critical layer damping of the Kelvin mode A. The inviscid limit is peculiar

https://doi.org/10.1017/jfm.2016.533 Published online by Cambridge University Press

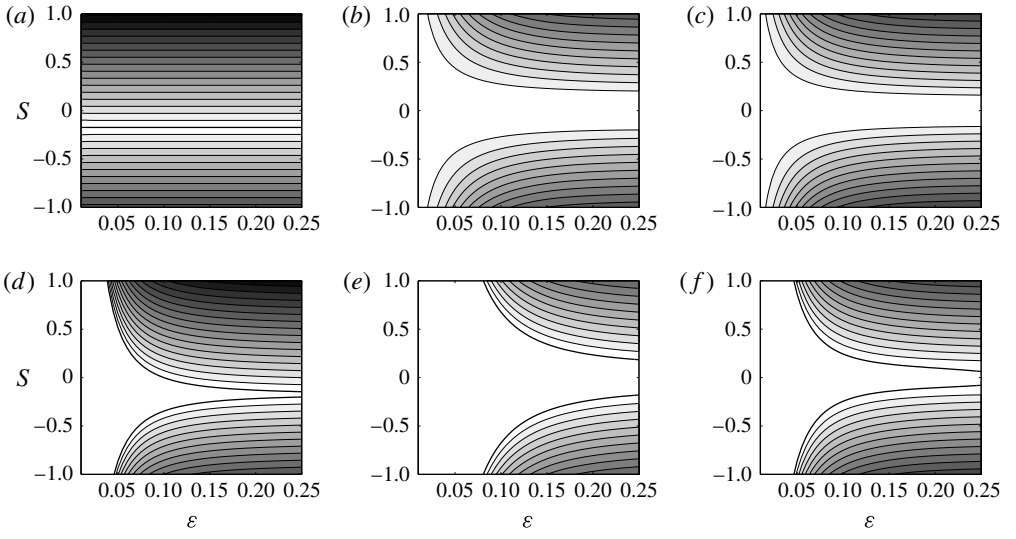


FIGURE 6. Contour levels of the maximum instability growth rate $\sigma_{max}/\varepsilon^2$ in the (ε, S) plane for $Re=\infty$ (*a–c*) and $Re=5000$ (*d–f*). (*a*,*d*) Mode $(-1, 1, 1)$ for $W_0=0$, (*b*,*e*) mode $(-2, 0, 2)$ for $W_0=0.2$, (*c*,*f*) mode $(-2, 0, 1)$ for $W_0=0.4$. Contours are every 0.1. The marginal curve ($\sigma_{max}=0$) is indicated by a thick solid line.

	$(-1, 1, 1)$ $(W_0=0)$	$(-2, 0, 2)$ $(W_0=0.2)$	$(-2, 0, 1)$ $(W_0=0.4)$
Q_A	-0.1418	$0.116+0.042\mathrm{i}$	$0.203+0.039\mathrm{i}$
Q_B	0.1418	-0.027	-0.039
V_A	-11.935	$-16.406-4.324\mathrm{i}$	$-3.646-1.264\mathrm{i}$
V_B	-11.935	-26.419	-6.605
$D_A^{(\varepsilon)}$	0.028	$-0.340-0.258\mathrm{i}$	$-0.342-0.174\mathrm{i}$
$D_B^{(\varepsilon)}$	-0.028	$-0.283+0.019\mathrm{i}$	$-0.155+0.016\mathrm{i}$
R_{AB}	-1.379	$3.464+1.212\mathrm{i}$	$1.151+0.191\mathrm{i}$
R_{BA}	1.379	$-0.412+0.020\mathrm{i}$	$-1.442+0.043\mathrm{i}$
$R_{AB}^{(\varepsilon)}$	-0.239	$0.542-0.027\mathrm{i}$	$0.128-0.019\mathrm{i}$
$R_{BA}^{(\varepsilon)}$	0.239	$-0.057+0.025\mathrm{i}$	$-0.152+0.052\mathrm{i}$

TABLE 2. Coefficients of the growth rate equation for the modes $(-1, 1, 1)$, $(-2, 0, 2)$ and $(-2, 0, 1)$ at the values $W_0=0$, 0.2 and 0.4, respectively.

because the domain of instability covers the entire parameter space. Only the mode $(-1, 1, 1)$ becomes marginal when $S\approx-0.1735$. The modes $(-2, 0, 1)$ and $(-2, 0, 2)$ are unstable for all values of S but their growth rate is very weak in a large region of the parameter space.

As soon as viscosity is present, a threshold in ε appears for instability to occur. This threshold increases as Re decreases. For $Re=5000$, it is already important, as observed in figure 6(*d–f*). For $\varepsilon=0.25$, viscosity has stabilized the mode $(-1, 1, 1)$ in $-0.2<S<-0.15$, the mode $(-2, 0, 2)$ in $-0.18<S<0.18$ and the mode $(-2, 0, 1)$ in $-0.08<S<0.06$. It should be noted that the viscous damping is stronger on the mode $(-2, 0, 2)$ (*b*,*e*) than on the other modes, as expected from the larger value of the resonant wavenumber of this mode (see table 1).

https://doi.org/10.1017/jfm.2016.533 Published online by Cambridge University Press

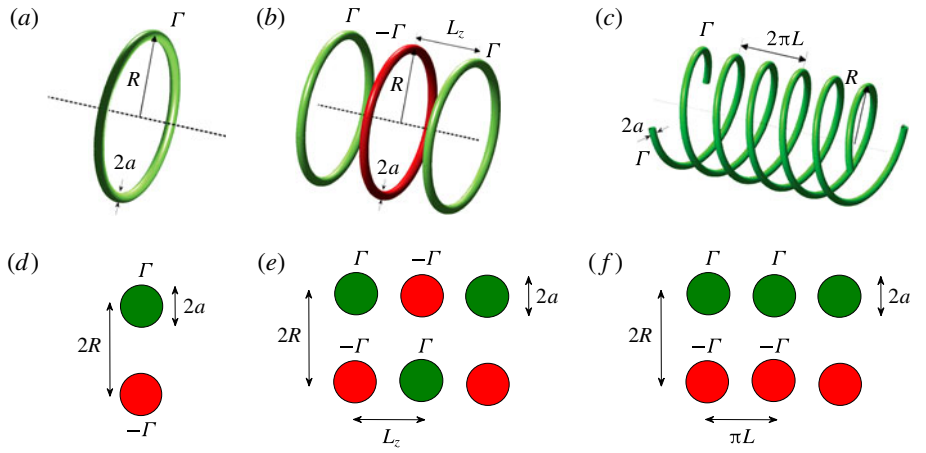


FIGURE 7. (Colour online) Sketch of the considered vortex structures. Curved (*a–c*) and equivalent straight (*d–f*) configurations. From left to right: a single vortex ring (two counter-rotating vortices), an array of alternate vortex rings (a double array of alternate vortices) and two helices (a double array of co-rotating vortices).

8. Applications

In this section, we apply the results to three different configurations: a single ring, an array of alternate vortex rings and a system of 2 helices as illustrated in figure 7. Each configuration is compared to the equivalent straight configuration, that is a counter-rotating vortex pair, a double array of alternate vortex pairs and a double array of co-rotating vortices, respectively (see figure 7). For both curved and straight configurations, we consider the three different values $W_0 = 0,\ 0.2,\ 0.4$ for which we provide the maximum growth rate of the most unstable modes $(-1,\ 1,\ 1)$, $(-2,\ 0,\ 2)$ and $(-2,\ 0,\ 1)$, respectively.

8.1. *Vortex ring*

For a single ring of radius R and vortex core radius a, the parameter S is given by Blanco-Rodriguez *et al.* (2015)

$$S = S^{Ri} = -\frac{3}{16}\left[\log\left(\frac{8}{\varepsilon}\right) - \frac{4}{3}\right], \tag{8.1}$$

where $\varepsilon = a/R$. For a given value of the jet parameter W_0, the non-dimensionalized elliptic instability growth rate σ_{max} is a function of ε only. In figure 8(*a*), we have plotted $\sigma_{max}/\varepsilon^2$, that is the dimensional growth rate σ^*_{max} normalized by $\Gamma/(2\pi R^2)$ for $W_0 = 0,\ 0.2$ and 0.4 and two values of the Reynolds number. Figure 8(*a*) has to be compared with the same plot for 2 straight counter-rotating vortices distant of $2R$ (figure 8*b*). We clearly see by comparing these figures that curvature enhances the elliptic instability growth rate. This increase is mainly due to a larger local strain field felt by the vortex ring. In particular, this strain field varies as $\varepsilon^2\log(\varepsilon)$ for small ε which explains the divergence of the normalized inviscid growth rate of the mode $(-1,\ 1,\ 1)$ for small ε in figure 8(*a*). For the other two modes, the inviscid instability growth rate goes to zero for small ε due the critical layer damping of the mode A.

https://doi.org/10.1017/jfm.2016.533 Published online by Cambridge University Press

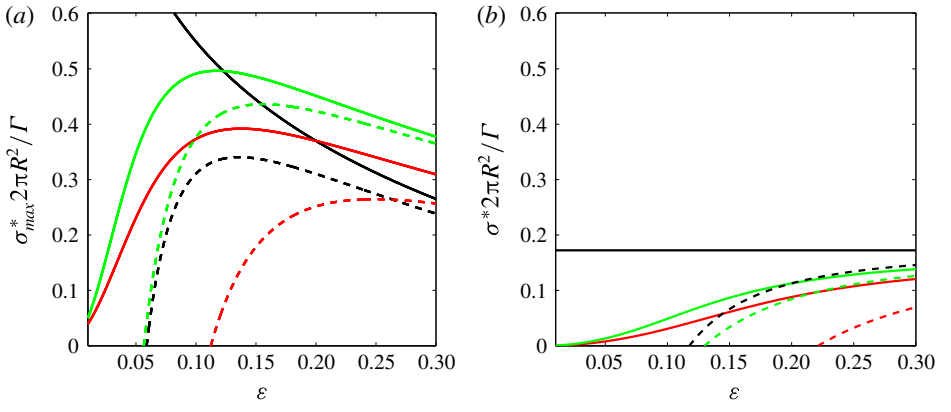


FIGURE 8. (Colour online) Maximum elliptic instability growth rate $\sigma_{max}/\varepsilon^2 = \sigma^*_{max}2\pi R^2/\Gamma$ versus $\varepsilon = a/R$ for a vortex ring of radius R (a) and 2 counter-rotating vortices distant of $2R$ (b), both of core size a. Black lines: $W_0 = 0$ (mode $(-1, 1, 1)$), red lines: $W_0 = 0.2$ (mode $(-2, 0, 2)$), green lines: $W_0 = 0.4$ (mode $(-2, 0, 1)$). Solid lines are for $Re = \infty$, dashed lines for $Re = 5000$. For both cases, the perturbation wavenumber is assumed not to be discretized (see figure 9).

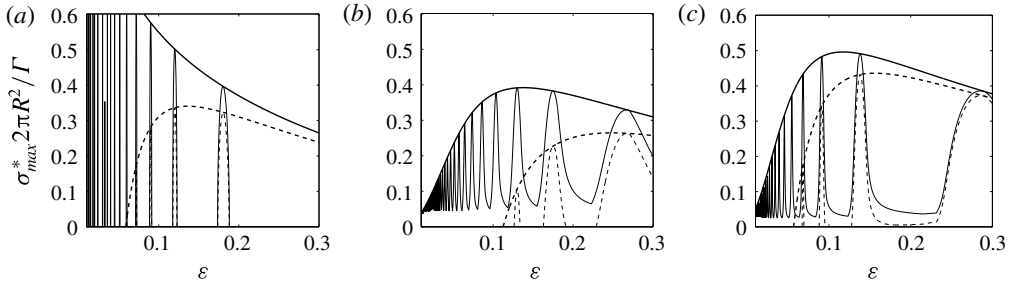


FIGURE 9. Elliptic instability growth rate $\sigma_{max}/\varepsilon^2 = \sigma^*_{max}2\pi R^2/\Gamma$ for a vortex ring of radius $R = 1/\varepsilon$ for $Re = \infty$ (solid lines) and $Re = 5000$ (dashed lines). Thick lines are the maximum growth rate curves plotted in figure 8(a), thin lines are the growth rate curves assuming that the instability wavenumbers are discretized and only take the values $k_n = 2\pi n\varepsilon$, $n = 1, 2, 3, \ldots$. (a) $W_0 = 0$ (mode $(-1, 1, 1)$), (b) $W_0 = 0.2$ (mode $(-2, 0, 2)$), (c) $W_0 = 0.4$ (mode $(-2, 0, 1)$).

In the presence of viscosity, there is an instability threshold in ε for each mode. The instability threshold is larger for the straight vortices than for the ring.

Figure 8(a) does not take into account that for a ring, the axial wavenumber is discretized and can only take the values $k_n = 2\pi n/R$, $n = 1, 2, 3, \ldots$, that is $k_n = 2\pi n\varepsilon$ when non-dimensionalized by the core radius. If we take into account this constraint we obtain the growth rate curves shown in figure 9. As can be seen on this figure, the discretization of the wavenumber has a strong influence. Without axial flow, the vortex ring is found to be unstable in short intervals of ε only. A similar stabilizing effect is observed in the presence of axial flow but if the Reynolds number is sufficiently large, the growth rate remains positive. This is a consequence of the destabilizing effect of the curvature on one of the Kelvin modes when $W_0 \neq 0$, which was already noted above. It is worth mentioning that the elliptic instability does not necessarily

https://doi.org/10.1017/jfm.2016.533 Published online by Cambridge University Press

disappear when the growth rate of the mode that we have considered vanishes. Instead, we expect the growth of other modes associated with different wavenumbers.

For the first mode ((−1, 1, 1) at $W_0 = 0$), our results can be compared to those obtained by Widnall & Tsai (1977) for a Rankine vortex profile. In the inviscid limit, they obtained with our normalization $\sigma_{max}/\varepsilon^2 = [(0.214 \log(8/\varepsilon) - 0.228)^2 - 0.028]^{1/2}$. For the Batchelor vortex with $W_0 = 0$ (that is the Lamb–Oseen vortex), we obtain $\sigma_{max}/\varepsilon^2 = (0.2585 \log(8/\varepsilon) - 0.5841)$. The third stabilizing term which is present in the Widnall & Tsai formula corresponds to a detuning effect associated with the coefficients $D_A^{(\varepsilon)}$ and $D_B^{(\varepsilon)}$. This term can be cancelled by slightly modifying the axial wavenumber of the resonant waves, an operation that was not performed by Widnall & Tsai. If we suppress this term, the elliptic instability growth rate of the Lamb–Oseen vortex ring is then found to be smaller than of a Rankine vortex ring as soon as $\varepsilon > 0.003$. This comes from a stronger stabilizing effect of the curvature on the Lamb–Oseen vortex because for straight vortices the opposite result can be proved (Eloy & Le Dizès 1999).

8.2. *Array of alternate vortex rings*

We consider an array of alternate vortex rings of radius R and separated by a distance L_z (see figure 7). Adapting the results of Blanco-Rodriguez *et al.* (2015) obtained for an array of identical rings, we immediately get for an array of ring of alternate signs

$$S = S^{Ri} + S^{DRi}, \tag{8.2}$$

where S^{Ri} is given by (8.1) and

$$S^{DRi} = \frac{1}{4}\sum_{n=1}^{\infty}(-1)^n \Lambda_n^{3/2}\left(\left(1 - \frac{4}{n^2\lambda^2}\right)\boldsymbol{E}(\Lambda_n) - \boldsymbol{K}(\Lambda_n)\right), \tag{8.3}$$

with

$$\Lambda_n = \left(1 + \frac{n^2 L_z^2}{4R^2}\right)^{-1}, \tag{8.4}$$

where $\boldsymbol{K}(Z)$ and $\boldsymbol{E}(Z)$ are complete elliptic integrals of the first and second kind, respectively.

Contrary to vortex rings of the same sign, rings of alternate sign can provide a strain parameter S that can vanish. For $\varepsilon = a/R = 0.1$, S vanishes for $L_z/R \approx 1.368$. In figure 10, we have plotted the maximum inviscid growth rate of the elliptic instability modes documented above for an array of alternate vortex rings and for the equivalent configuration with straight vortices (array of straight counter-rotating vortex pairs of alternate sign). For large L_z/R, the growth rate curves converge to the values obtained for a single ring and for a single vortex pair (which is that obtained for $a/R = 0.1$ in figure 8). For small L_z/R, both configurations provide the same growth rates, that of a single array of straight vortices of alternate sign. Note however that a/L_z must remain small for the asymptotic solution to be valid. The results of figure 10 obtained for $a/R = 0.1$ are therefore not expected to apply for L_z/R smaller than approximately 0.5.

Note, finally, that the discretization of the instability wavenumber in an array of rings, which has not been taken into account in figure 10, is similar to that of a single ring. We have assumed that the maximum growth rate was reached for $\varepsilon = 0.1$ for the three cases. This is not true. A particular value of ε exists close to 0.1 where the maximum growth rate is reached but it is actually different for each mode. For the first case (mode (−1, 1, 1) at $W_0 = 0$), this occurs for $\varepsilon = 0.12$, while it is $\varepsilon = 0.104$ and $\varepsilon = 0.091$ for the second and third cases (mode (−2, 0, 2) at $W_0 = 0.2$ and mode (−2, 0, 1) at $W_0 = 0.4$, respectively).

https://doi.org/10.1017/jfm.2016.533 Published online by Cambridge University Press

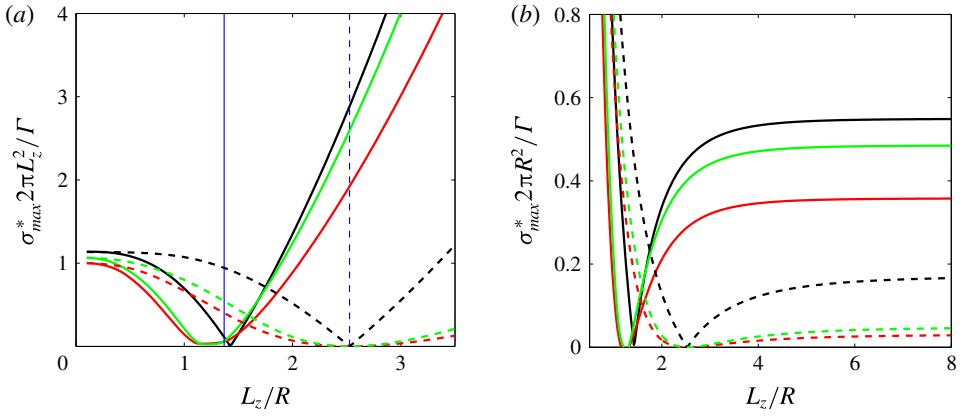


FIGURE 10. (Colour online) Maximum elliptic instability growth rate versus L_z/R of an array of alternate vortex rings (solid lines) and of an array of straight counter-rotating vortex pairs of alternate sign (dashed lines) for $\varepsilon = a/R = 0.1$ and $Re = \infty$. Black lines: $W_0 = 0$ (mode $(-1, 1, 1)$), red lines: $W_0 = 0.2$ (mode $(-2, 0, 2)$), green lines: $W_0 = 0.4$ (mode $(-2, 0, 1)$). (*a*) Normalization with $\Gamma/(2\pi L_z^2)$. (*b*) Normalization with $\Gamma/(2\pi R^2)$. The vertical lines on (*a*) indicate the value of L_z/R where the local strain rate vanishes for each configuration.

8.3. *Two helical vortices*

Blanco-Rodriguez *et al.* (2015) have obtained an expression of the strain parameter for N helical Batchelor vortices of radius R and pitch L. For $N = 2$, their expression reduces to

$$S^{MHe} = -\frac{3}{16}\log\left(\frac{\alpha}{(\alpha^2+1)^{3/2}2\varepsilon}\right) - \frac{16(\alpha^2+1)^3 + \alpha^2(20\alpha^4+12\alpha^2+9)}{96\alpha^2} + \frac{1}{2}\alpha(\alpha^2+1)^{3/2} + \sum_{m=1}^{\infty} S_m(\alpha) \tag{8.5}$$

with

$$\alpha = \frac{L}{R}, \quad \varepsilon = \frac{Ra}{R^2+L^2}, \tag{8.6a,b}$$

and

$$S_m(\alpha) = \alpha(\alpha^2+1)^{3/2} + \frac{3}{16m} - \frac{2(1+\alpha^2)^3 m}{\alpha^2} + \frac{8m^2(\alpha^2+1)^{5/2}}{\alpha^3} \times \left(-I_{2m-1}\left(\frac{2m}{\alpha}\right) + \alpha I_{2m}\left(\frac{2m}{\alpha}\right)\right)\left(K_{2m-1}\left(\frac{2m}{\alpha}\right) + \alpha K_{2m}\left(\frac{2m}{\alpha}\right)\right) + 4m(\alpha^2+1)^{3/2} I_{2m}\left(\frac{2m}{\alpha}\right)\left(K_{2m-1}\left(\frac{2m}{\alpha}\right) + \alpha K_{2m}\left(\frac{2m}{\alpha}\right)\right), \tag{8.7}$$

where $K_n(z)$ and $I_n(z)$ are modified Bessel functions.

As for alternate rings, the strain rate parameter S can vanish for particular values of α. This leads to a drop in the elliptic instability growth rate. In figure 11, we have plotted the maximum inviscid growth rate as a function of L/R for $a/R = 0.1$ for the

https://doi.org/10.1017/jfm.2016.533 Published online by Cambridge University Press

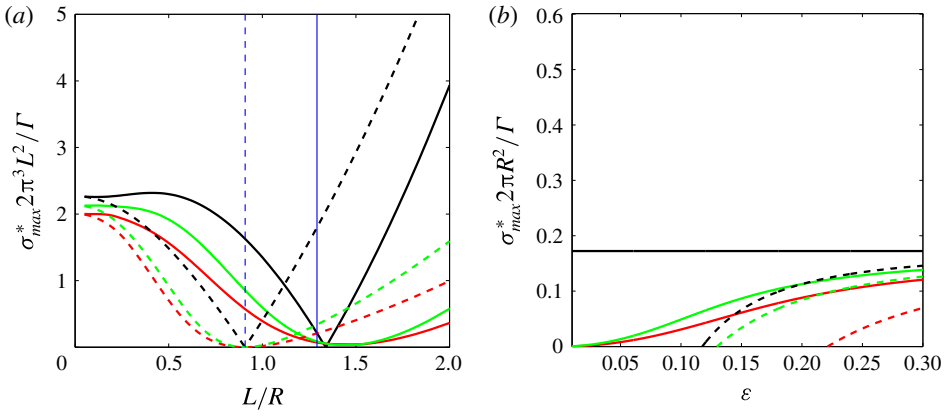


FIGURE 11. (Colour online) Maximum elliptic instability growth rate versus L/R of two helical vortices (solid lines) and of an double array of straight co-rotating vortices (dashed lines) for $a/R = 0.1$ and $Re = \infty$. Black lines: $W_0 = 0$ (mode $(-1, 1, 1)$), red lines: $W_0 = 0.2$ (mode $(-2, 0, 2)$), green lines: $W_0 = 0.4$ (mode $(-2, 0, 1)$). (a) Normalization with $\Gamma/(2\pi^3 L^2)$. (b) Normalization with $\Gamma/(2\pi R^2)$. The vertical lines on (a) indicate the value of L/R where the local strain rate vanishes for each configuration.

three different modes already considered for the ring. The growth rate of the helical vortex configuration is compared to the equivalent 'straight' configuration obtained by considering a longitudinal cut of the helical configuration, that is a double array of co-rotating vortices (see figure 7). We observe that for small L/R and for large L/R, both configurations give the same growth rates, which are that of a single array of straight co-rotating vortices and of a straight vortex pair. For intermediate values of L/R, the curves of straight and helical configurations exhibit the same qualitative behaviour: the inviscid growth rate of the mode $(-1, 1, 1)$ vanishes at a single value of L/R, while the modes $(-2, 0, 2)$ and $(-2, 0, 1)$ are stabilized in a finite interval of L/R. However, the numerical values for both configurations are very different. The point of vanishing of the inviscid growth rate of the mode $(-1, 1, 1)$ occurs at the place where the local strain field felt by the vortex vanishes for the straight configuration. It is slightly shifted to a smaller value for the helical configuration: this is an effect of the additional contribution to the growth rate due to curvature. For $L/R \gtrsim 1$, the straight configuration is found to be more unstable than the helical one, while it is the opposite for $L/R \lesssim 1$.

As for the ring arrays, we have to keep in mind that L/R is *a priori* of $O(1)$ in the asymptotic analysis. Small values of L/R can be considered as long as a/L remains also small. In figure 11, this constraint requires L/R to be much larger than 0.1.

9. Conclusion

In this work, we have analysed the elliptic instability in a strained and curved Batchelor vortex using the framework initially developed by Moore & Saffman (1975). We have focused on the combinations of resonant Kelvin modes expected to be the most unstable for moderate Reynolds numbers, which are the principal modes $(-1, 1, 1)$, $(-2, 0, 2)$ and $(-2, 0, 1)$. Expressions for the elliptic instability growth rate of these principal modes have been obtained as a function of the jet parameter. The effect of the local curvature of the vortex has been included. While curvature does not modify the instability mode structure at leading order, it changes the growth rate

https://doi.org/10.1017/jfm.2016.533 Published online by Cambridge University Press

by modifying the local strain field felt by the vortex and by adding a supplementary contribution. This additional contribution turns out to be in general small compared to the strain field contribution. A few situations (array of alternate vortex rings, pair of helices of particular pitch) have been identified where this contribution becomes dominant.

In the analysis, we have assumed that the vortical structure is stationary in a moving frame. When the moving frame is rotating, Coriolis effects are expected. These effects have not been considered in the present analysis. For the configurations that we have studied, the angular rotation is asymptotically small (of order $\varepsilon^2 S$ or $\varepsilon \log \varepsilon$), so Coriolis effects remain small. These effects can still be computed, as shown in Le Dizès & Laporte (2002) and Roy *et al.* (2008), for straight vortex pairs without and with axial flows, respectively.

A curved vortex can *a priori* be unstable with respect to the curvature instability (Fukumoto & Hattori 2005; Hattori & Fukumoto 2014). This instability is also associated with a resonance mechanism of Kelvin modes but with the condition of resonance $m_A = m_B + 1$, $k_A = k_B$ and $\omega_A = \omega_B$. If this condition is met for the Kelvin modes of the Batchelor vortex, the curvature instability is expected to be active. The curvature instability could then be stronger than the elliptic instability described in the present paper. This is probably not the case for configurations without a jet for moderate Reynolds numbers, as experiments tend to demonstrate (Widnall & Tsai 1977), but this may occur in the presence of a sufficiently strong jet (Leweke *et al.* 2014).

Finally, note that helical vortices are also subject to a long-wave instability (Widnall 1972) which distorts the helical structure. This instability leads to the local pairing of two successive loops. It could enhance the elliptic instability in the regions where the vortex loops get closer owing to the local increase of the strain field as already observed for the Crow instability (Laporte & Corjon 2000; Leweke *et al.* 2016).

Acknowledgements

This work received support from the French Agence Nationale de la Recherche under the A*MIDEX grant ANR-11-IDEX-0001-02, the LABEX MEC project ANR-11-LABX-0092 and the ANR HELIX project ANR-12-BS09-0023-01.

Appendix A. Base flow expressions

In this section, we recall the expression of the base flow as obtained in Blanco-Rodriguez *et al.* (2015).

The dipolar correction is written as

$$\boldsymbol{U}_d \sim \varepsilon\, Re(\boldsymbol{U}^{(1)} \mathrm{e}^{\mathrm{i}\varphi}) = \frac{\varepsilon}{2} \begin{pmatrix} \mathrm{i}U^{(1)}(r) \\ V^{(1)}(r) \\ W^{(1)}(r) \\ P^{(1)}(r) \end{pmatrix} \mathrm{e}^{\mathrm{i}\varphi} + \text{c.c.}, \tag{A 1}$$

where

$$U^{(1)} = \frac{\Psi^{(1)}}{r}, \tag{A 2a}$$

$$V^{(1)} = (-\Psi_r^{(1)} + rV^{(0)}), \tag{A 2b}$$

https://doi.org/10.1017/jfm.2016.533 Published online by Cambridge University Press

$$W^{(1)} = \left(-\frac{W_r^{(0)}}{V^{(0)}} \Psi^{(1)} + r W^{(0)} \right), \tag{A 2c}$$

$$P^{(1)} = (-\zeta^{(0)} \Psi^{(1)} + V^{(0)} \Psi_r^{(1)} - r[V^{(0)}]^2 - r[W^{(0)}]^2), \tag{A 2d}$$

with

$$\Psi^{(1)}(r) = V^{(0)}(r) \int_0^r \frac{\displaystyle\int_0^z V^{(0)}(\eta) \left[2\eta \zeta^{(0)}(\eta) + V^{(0)}(\eta) + 2\eta \frac{W^{(0)}(\eta) W_r^{(0)}(\eta)}{V^{(0)}(\eta)} \right] \eta \, \mathrm{d}\eta}{z[V^{(0)}(z)]^2} \, \mathrm{d}z. \tag{A 3}$$

In these expressions, $\zeta^{(0)}(r) = 2\mathrm{e}^{-r^2}$ is the axial vorticity of the Batchelor vortex.

The quadripolar field is written as

$$\boldsymbol{U}_q \sim \varepsilon^2 \, Re((S\boldsymbol{U}^{(2)} + \boldsymbol{U}_\varepsilon^{(2)}) \mathrm{e}^{2\mathrm{i}\varphi}) = \frac{\varepsilon^2}{2} \left\{ S \begin{pmatrix} \mathrm{i}U^{(2)}(r) \\ V^{(2)}(r) \\ W^{(2)}(r) \\ P^{(2)}(r) \end{pmatrix} + \begin{pmatrix} \mathrm{i}U_\varepsilon^{(2)}(r) \\ V_\varepsilon^{(2)}(r) \\ W_\varepsilon^{(2)}(r) \\ P_\varepsilon^{(2)}(r) \end{pmatrix} \right\} \mathrm{e}^{2\mathrm{i}\varphi} + \mathrm{c.c.}, \tag{A 4}$$

where the first part is given by

$$U^{(2)} = \frac{2}{r} \Psi^{(2)}, \tag{A 5a}$$

$$V^{(2)} = -\partial_r \Psi^{(2)}, \tag{A 5b}$$

$$W^{(2)} = -\frac{\partial_r W^{(0)}}{V^{(0)}} \Psi^{(2)}, \tag{A 5c}$$

$$P^{(2)} = -\zeta^{(0)} \Psi^{(2)} + V^{(0)} \partial_r \Psi^{(2)}, \tag{A 5d}$$

with $\Psi^{(2)}(r)$ satisfying

$$\left[\frac{\partial^2}{\partial r^2} + \frac{1}{r} \frac{\partial}{\partial r} - \left(\frac{4}{r^2} + \frac{\partial_r \zeta^{(0)}}{V^{(0)}} \right) \right] \Psi^{(2)} = 0; \quad \Psi^{(2)} \underset{r \to +\infty}{\sim} r^2, \tag{A 6}$$

and the second part by

$$U_\varepsilon^{(2)} = \frac{2}{r} \Psi_\varepsilon^{(2)}, \tag{A 7a}$$

$$V_\varepsilon^{(2)} = -\partial_r \Psi_\varepsilon^{(2)} + V_F, \tag{A 7b}$$

$$W_\varepsilon^{(2)} = -\frac{\partial_r W^{(0)}}{V^{(0)}} \Psi_\varepsilon^{(2)} + W_F, \tag{A 7c}$$

$$P_\varepsilon^{(2)} = -\zeta^{(0)} \Psi_\varepsilon^{(2)} + V^{(0)} \partial_r \Psi_\varepsilon^{(2)} + P_F, \tag{A 7d}$$

with

$$\Psi_\varepsilon^{(2)} = \Psi^{(2)} \left[\frac{3}{16} \log r - \int_r^{+\infty} \left(\frac{\displaystyle\int_0^s \eta \mathscr{F}(\eta) \Psi^{(2)}(\eta) \, \mathrm{d}\eta}{s[\Psi^{(2)}]^2} - \frac{3}{16s} \right) \mathrm{d}s \right], \tag{A 8a}$$

$$\mathscr{F} = \frac{3rV^{(0)}}{4} - \frac{r\Psi^{(1)} \zeta_r^{(0)}}{V^{(0)}} - \frac{(\Psi^{(1)})^2}{4V^{(0)}} \left(\frac{\zeta_r^{(0)}}{V^{(0)}} \right)_r + \frac{r\Psi^{(1)}}{[V^{(0)}]^2} \left[\frac{W^{(0)} W_r^{(0)} V_r^{(0)}}{V^{(0)}} - (W^{(0)} W_r^{(0)})_r \right], \tag{A 8b}$$

https://doi.org/10.1017/jfm.2016.533 Published online by Cambridge University Press

and

$$V_F = \frac{r^2}{4}(U_r^{(1)} + 2V^{(0)}), \tag{A 9a}$$

$$W_F = \frac{r}{4V^{(0)}}\left[-\frac{W^{(1)}V^{(1)}}{r} + W_r^{(1)}U^{(1)} + V^{(0)}(W^{(1)} + rW^{(0)}) + W^{(0)}(V^{(1)} - U^{(1)})\right], \tag{A 9b}$$

$$P_F = \frac{r}{4}U^{(1)}V_r^{(1)} - \frac{V^{(1)}}{4}(V^{(1)} - U^{(1)}) - \frac{r}{2}W^{(0)}\left(W^{(1)} + \frac{r}{2}W^{(0)}\right) - V^{(0)}V_F. \tag{A 9c}$$

The second part is such that $\Psi_\varepsilon^{(2)} \sim (3/16)r^2 \log r + O(r)$ as $r \to \infty$. It corresponds to the particular solution for which the external strain contribution proportional to r^2 has been cancelled out. The solution associated with the external strain field is the first part.

Appendix B. Operators

The operators appearing in (3.2) are given by

$$\boldsymbol{I} = \begin{bmatrix} 1 & 0 & 0 & 0 \\ 0 & 1 & 0 & 0 \\ 0 & 0 & 1 & 0 \\ 0 & 0 & 0 & 0 \end{bmatrix}, \quad \boldsymbol{P} = \begin{bmatrix} W^{(0)} & 0 & 0 & 0 \\ 0 & W^{(0)} & 0 & 0 \\ 0 & 0 & W^{(0)} & 1 \\ 0 & 0 & -1 & 0 \end{bmatrix}, \tag{B 1a,b}$$

$$\boldsymbol{M}(-\mathrm{i}\partial_\varphi) = \begin{bmatrix} \Omega^{(0)}\,\mathrm{i}\partial_\varphi & -2\,\Omega^{(0)} & 0 & \partial_r \\ -\zeta^{(0)} & \Omega^{(0)}\,\mathrm{i}\partial_\varphi & 0 & \dfrac{\mathrm{i}}{r}\partial_\varphi \\ -W_r^{(0)} & 0 & \Omega^{(0)}\,\mathrm{i}\partial_\varphi & 0 \\ \dfrac{1}{r} + \partial_r & -\dfrac{\mathrm{i}}{r}\partial_\varphi & 0 & 0 \end{bmatrix}, \tag{B 2}$$

$$\boldsymbol{V}(-\mathrm{i}\partial_\varphi, -\mathrm{i}\partial_s) = \begin{bmatrix} \Delta - \dfrac{1}{r^2} & \dfrac{2\mathrm{i}}{r^2}\partial_\varphi & 0 & 0 \\ \dfrac{2\mathrm{i}}{r^2}\partial_\varphi & \Delta - \dfrac{1}{r^2} & 0 & 0 \\ 0 & 0 & \Delta & 0 \\ 0 & 0 & 0 & 0 \end{bmatrix}, \tag{B 3}$$

$$\boldsymbol{N}_\pm^{(1)}(-\mathrm{i}\partial_\varphi, -\mathrm{i}\partial_s) = \frac{1}{2}\begin{bmatrix} D_\pm^{(1)} \pm U_r^{(1)} & \dfrac{U^{(1)}}{r} + 2\dfrac{V^{(1)}}{r} & -2W^{(0)} & 0 \\ V_r^{(1)} + \dfrac{V^{(1)}}{r} & D_\pm^{(1)} \pm \dfrac{V^{(1)}}{r} \pm \dfrac{U^{(1)}}{r} & \pm 2W^{(0)} & 0 \\ W_r^{(1)} - W^{(0)} & \pm\dfrac{W^{(1)}}{r} \mp W^{(0)} & D_\pm^{(1)} \mp V^{(0)} & -r\mathrm{i}\partial_s \\ 1 & \pm 1 & r\mathrm{i}\partial_s & 0 \end{bmatrix}, \tag{B 4}$$

https://doi.org/10.1017/jfm.2016.533 Published online by Cambridge University Press

$$\boldsymbol{N}_{\pm}^{(2)}(-\mathrm{i}\partial_\varphi,-\mathrm{i}\partial_s)=\frac{1}{2}\begin{bmatrix} D_{\pm}^{(2)}\pm U_r^{(2)} & 2\dfrac{U^{(2)}}{r}+2\dfrac{V^{(2)}}{r} & 0 & 0\\ V_r^{(2)}+\dfrac{V^{(2)}}{r} & D_{\pm}^{(2)}\pm 2\dfrac{V^{(2)}}{r}\pm\dfrac{U^{(2)}}{r} & 0 & 0\\ W_r^{(2)} & \pm 2\dfrac{W^{(2)}}{r} & D_{\pm}^{(2)} & 0\\ 0 & 0 & 0 & 0\end{bmatrix}, \tag{B 5}$$

$$\boldsymbol{N}_{\varepsilon\pm}^{(2)}(-\mathrm{i}\partial_\varphi,-\mathrm{i}\partial_s)=\frac{1}{2}\begin{bmatrix} D_{\varepsilon\pm}^{(2)}\pm\partial_r U_\varepsilon^{(2)} & 2\dfrac{U_\varepsilon^{(2)}}{r}+2\dfrac{V_\varepsilon^{(2)}}{r} & -T_w & 0\\ \partial_r V_\varepsilon^{(2)}+\dfrac{V_\varepsilon^{(2)}}{r} & D_{\varepsilon\pm}^{(2)}\pm 2\dfrac{V_\varepsilon^{(2)}}{r}\pm\dfrac{U_\varepsilon^{(2)}}{r} & \pm T_w & 0\\ \partial_r W_\varepsilon^{(2)}-\dfrac{T_w}{2} & \pm 2\dfrac{W_\varepsilon^{(2)}}{r}\mp\dfrac{T_w}{2} & D_{\varepsilon\pm}^{(2)}\mp\dfrac{T_v}{2}\mp\dfrac{U^{(1)}}{2} & -\dfrac{r^2}{2}\mathrm{i}\partial_s\\ \dfrac{r}{2} & \pm\dfrac{r}{2} & \dfrac{r^2}{2}\mathrm{i}\partial_s & 0\end{bmatrix}, \tag{B 6}$$

$$\boldsymbol{D}(-\mathrm{i}\partial_s)=\frac{1}{2}\begin{bmatrix} -\dfrac{T_w r}{2}\mathrm{i}\partial_s & 0 & -T_w & 0\\ 0 & -\dfrac{T_w r}{2}\mathrm{i}\partial_s & 0 & 0\\ -\dfrac{T_w}{2} & 0 & -\dfrac{T_w r}{2}\mathrm{i}\partial_s & -\dfrac{r^2}{2}\mathrm{i}\partial_s\\ \dfrac{r}{2} & 0 & \dfrac{r^2}{2}\mathrm{i}\partial_s & 0\end{bmatrix}, \tag{B 7}$$

where $\Omega^{(0)}=V^{(0)}/r$ and

$$D_{\pm}^{(1)}=\pm U^{(1)}\,\partial_r-\frac{V^{(1)}}{r}\,\mathrm{i}\partial_\varphi-(W^{(1)}+rW^{(0)})\,\mathrm{i}\partial_s, \tag{B 8a}$$

$$D_{\pm}^{(2)}=\pm U^{(2)}\,\partial_r-\frac{V^{(2)}}{r}\,\mathrm{i}\partial_\varphi-W^{(2)}\,\mathrm{i}\partial_s, \tag{B 8b}$$

$$D_{\varepsilon\pm}^{(2)}=\pm U_\varepsilon^{(2)}\,\partial_r-\frac{V_\varepsilon^{(2)}}{r}\,\mathrm{i}\partial_\varphi-\left(W_\varepsilon^{(2)}+\frac{r}{2}W^{(1)}+\frac{r^2}{2}W^{(0)}\right)\mathrm{i}\partial_s, \tag{B 8c}$$

$$T_w=W^{(1)}+rW^{(0)}, \tag{B 8d}$$

$$T_v=V^{(1)}+rV^{(0)}, \tag{B 8e}$$

$$\Delta=\partial_r^2+\frac{1}{r}\partial_r+\frac{1}{r^2}\partial_\varphi^2+\partial_s^2. \tag{B 8f}$$

Appendix C. Formulae for the coefficients of the growth rate expression

In this section, we provide approximations for the coefficients appearing in the growth rate equation (4.7) for the modes $(-1,1,1)$, $(-2,0,2)$ and $(-2,0,1)$. These expressions can be used in a finite interval of the axial flow parameter W_0 which is different for each mode.

For the mode $(-1,1,1)$, we can use the following formula in the interval $0\leqslant W_0<0.3$:

$$k_c=-3.74W_0^2-0.68W_0+2.28, \tag{C 1a}$$

https://doi.org/10.1017/jfm.2016.533 Published online by Cambridge University Press

$$\omega_c = -1.77W_0^2 + 1.03W_0, \tag{C 1b}$$
$$\mathrm{Im}(\omega_B) = -0.17W_0 + 0.03, \quad W_0 > 0.176, \tag{C 1c}$$
$$Q_A = 0.87W_0 + 0.14, \tag{C 1d}$$
$$\mathrm{Re}(Q_B) = -1.42W_0^2 + 0.87W_0 - 0.145, \tag{C 1e}$$
$$\mathrm{Im}(Q_B) = 0.1445W_0 - 0.018, \quad W_0 > 0.125, \tag{C 1f}$$
$$V_A = 60.94W_0^2 - 31.25W_0 - 12.4, \tag{C 1g}$$
$$\mathrm{Re}(V_B) = 41.38W_0 - 11.64, \tag{C 1h}$$
$$\mathrm{Im}(V_B) = 32.4W_0 - 3.915, \quad W_0 > 0.121, \tag{C 1i}$$
$$\mathrm{Re}(D_A^{(\varepsilon)}) = 2.43W_0^2 - 1.24W_0 + 0.03, \tag{C 1j}$$
$$\mathrm{Im}(D_A^{(\varepsilon)}) = -1.28W_0^2 + 0.59W_0, \tag{C 1k}$$
$$\mathrm{Re}(D_B^{(\varepsilon)}) = 9.42W_0^2 - 1.53W_0 - 0.05, \tag{C 1l}$$
$$\mathrm{Im}(D_B^{(\varepsilon)}) = -2.75W_0, \tag{C 1m}$$
$$\mathrm{Re}(R_{AB}) = 19.8W_0^2 - 10.4W_0 - 1.35, \tag{C 1n}$$
$$\mathrm{Im}(R_{AB}) = -1.39W_0 + 0.2076, \quad W_0 > 0.1488, \tag{C 1o}$$
$$\mathrm{Re}(R_{BA}) = 16.6W_0^2 - 9.55W_0 + 1.39, \tag{C 1p}$$
$$\mathrm{Im}(R_{BA}) = 5.03W_0^2 - 2.49W_0 + 0.241, \quad W_0 > 0.132, \tag{C 1q}$$
$$\mathrm{Re}(R_{AB}^{\varepsilon}) = 17W_0^2 - 3.94W_0 - 0.22, \tag{C 1r}$$
$$\mathrm{Im}(R_{AB}^{\varepsilon}) = 81.9W_0^3 - 35.4W_0^2 + 0.72W_0, \tag{C 1s}$$
$$\mathrm{Re}(R_{BA}^{\varepsilon}) = 2.83W_0^2 - 1.61W_0 + 0.245, \tag{C 1t}$$
$$\mathrm{Im}(R_{BA}^{\varepsilon}) = 11.7W_0^3 - 7.17W_0^2 + 1.11.W_0. \tag{C 1u}$$

For the mode $(-2,\ 0,\ 2)$, we can use the following formula in the interval $0.15 < W_0 < 0.35$:

$$k_c = -29.62W_0^2 + 16.23W_0 + 1.14, \tag{C 2a}$$
$$\omega_c = -1.82W_0^2 + 2.30W_0 - 0.74, \tag{C 2b}$$
$$\mathrm{Im}(\omega_A) = 1.26W_0 - 0.26, \quad W_0 < 0.206, \tag{C 2c}$$
$$\mathrm{Re}(Q_A) = 1.5W_0 - 0.175, \tag{C 2d}$$
$$\mathrm{Im}(Q_A) = -1.77W_0 + 0.393, \quad W_0 < 0.222, \tag{C 2e}$$
$$Q_B = -2.25W_0^2 + 1.52W_0 - 0.24, \tag{C 2f}$$
$$\mathrm{Re}(V_A) = 554.1W_0^2 - 435.8W_0 + 48.21, \tag{C 2g}$$
$$\mathrm{Im}(V_A) = 122.6W_0 - 28.84, \quad W_0 < 0.235, \tag{C 2h}$$
$$V_B = 50.82W_0 - 36.6, \tag{C 2i}$$
$$\mathrm{Re}(D_A^{(\varepsilon)}) = 308W_0^3 - 256W_0^2 + 68.9W_0 - 6.37, \tag{C 2j}$$
$$\mathrm{Im}(D_A^{(\varepsilon)}) = -18.4W_0^2 + 11.6W_0 - 1.83, \tag{C 2k}$$
$$\mathrm{Re}(D_B^{(\varepsilon)}) = 7.92W_0^2 - 5.48W_0 + 0.51, \tag{C 2l}$$
$$\mathrm{Im}(D_B^{(\varepsilon)}) = -0.154W_0 + 0.05, \tag{C 2m}$$
$$\mathrm{Re}(R_{AB}) = -720W_0^2 + 406W_0 - 49, \tag{C 2n}$$
$$\mathrm{Im}(R_{AB}) = -226W_0^2 + 77.7W_0 - 5.31, \quad W_0 < 0.250, \tag{C 2o}$$
$$\mathrm{Re}(R_{BA}) = -2.45W_0 + 0.861, \tag{C 2p}$$

https://doi.org/10.1017/jfm.2016.533 Published online by Cambridge University Press

$$\mathrm{Im}(R_{BA}) = -2.38W_0 + 0.452, \quad W_0 < 0.19, \tag{C 2q}$$
$$\mathrm{Re}(R^{\varepsilon}_{AB}) = 11.5W_0 - 1.66, \tag{C 2r}$$
$$\mathrm{Im}(R^{\varepsilon}_{AB}) = 13.6W_0^2 - 7.18W_0 + 0.87, \tag{C 2s}$$
$$\mathrm{Re}(R^{\varepsilon}_{BA}) = 0.81W_0^2 - 0.22W_0 - 0.035, \tag{C 2t}$$
$$\mathrm{Im}(R^{\varepsilon}_{BA}) = 1.22W_0^2 - 0.81W_0 + 0.13. \tag{C 2u}$$

For the mode $(-2, 0, 1)$, we can use the following formula in the interval $0.3 < W_0 < 0.5$:

$$k_c = -6.37W_0^2 + 7.89W_0 - 0.43, \tag{C 3a}$$
$$\omega_c = 1.54W_0^2 - 0.41W_0 - 0.4, \tag{C 3b}$$
$$\mathrm{Im}(\omega_A) = 0.33W_0 - 0.135, \quad W_0 < 0.409, \tag{C 3c}$$
$$\mathrm{Re}(Q_A) = 3.33W_0^2 - 1.22W_0 + 0.16, \tag{C 3d}$$
$$\mathrm{Im}(Q_A) = -0.665W_0 + 0.305, \quad W_0 < 0.459, \tag{C 3e}$$
$$Q_B = -2.13W_0^2 + 2.55W_0 - 0.72, \tag{C 3f}$$
$$\mathrm{Re}(V_A) = -81.18W_0^2 + 36.69W_0 - 5.379, \tag{C 3g}$$
$$\mathrm{Im}(V_A) = 19.7W_0 - 9.166, \quad W_0 < 0.465, \tag{C 3h}$$
$$V_B = 2.194W_0 - 7.37, \tag{C 3i}$$
$$\mathrm{Re}(D_A^{(\varepsilon)}) = -9.48W_0^2 + 9.5W_0 - 2.63, \tag{C 3j}$$
$$\mathrm{Im}(D_A^{(\varepsilon)}) = 1.35W_0 - 0.7, \tag{C 3k}$$
$$\mathrm{Re}(D_B^{(\varepsilon)}) = -0.51W_0 + 0.05, \tag{C 3l}$$
$$\mathrm{Im}(D_B^{(\varepsilon)}) = -0.07W_0 + 0.04, \tag{C 3m}$$
$$\mathrm{Re}(R_{AB}) = 44.3W_0^2 - 22.7W_0 + 3.13, \tag{C 3n}$$
$$\mathrm{Im}(R_{AB}) = -9.1W_0^2 + 5.17W_0 - 0.416, \quad W_0 < 0.471, \tag{C 3o}$$
$$\mathrm{Re}(R_{BA}) = 19.4W_0^2 - 25.5W_0 + 8.57, \tag{C 3p}$$
$$\mathrm{Im}(R_{BA}) = -13.3W_0^2 + 12.2W_0 - 2.798, \quad W_0 < 0.457, \tag{C 3q}$$
$$\mathrm{Re}(R^{\varepsilon}_{AB}) = 9.27W_0^2 - 5.63W_0 + 0.9, \tag{C 3r}$$
$$\mathrm{Im}(R^{\varepsilon}_{AB}) = -0.11W_0 + 0.03, \tag{C 3s}$$
$$\mathrm{Re}(R^{\varepsilon}_{BA}) = 0.5W_0 - 0.345, \tag{C 3t}$$
$$\mathrm{Im}(R^{\varepsilon}_{BA}) = 3.04W_0^2 - 3.29W_0 + 0.88. \tag{C 3u}$$

These expressions have been plotted in figures 2, 4 and 5.

REFERENCES

Blanco-Rodriguez, F. J., Le Dizès, S., Selçuk, C., Delbende, I. & Rossi, M. 2015 Internal structure of vortex rings and helical vortices. *J. Fluid Mech.* **785**, 219–247.

Callegari, A. J. & Ting, L. 1978 Motion of a curved vortex filament with decaying vortical core and axial velocity. *SIAM J. Appl. Maths* **35**, 148–175.

Crow, S. C. 1970 Stability theory for a pair of trailing vortices. *AIAA J.* **8** (12), 2172–2179.

Eloy, C. & Le Dizès, S. 1999 Three-dimensional instability of Burgers and Lamb–Oseen vortices in a strain field. *J. Fluid Mech.* **378**, 145–166.

Eloy, C. & Le Dizès, S. 2001 Stability of the Rankine vortex in a multipolar strain field. *Phys. Fluids* **13** (3), 660–676.

https://doi.org/10.1017/jfm.2016.533 Published online by Cambridge University Press

FABRE, D., SIPP, D. & JACQUIN, L. 2006 The Kelvin waves and the singular modes of the Lamb–Oseen vortex. *J. Fluid Mech.* **551**, 235–274.

FUKUMOTO, Y. 2003 The three-dimensional instability of a strained vortex tube revisited. *J. Fluid Mech.* **493**, 287–318.

FUKUMOTO, Y. & HATTORI, Y. 2005 Curvature instability of a vortex ring. *J. Fluid Mech.* **526**, 77–115.

HATTORI, Y. & FUKUMOTO, Y. 2014 Modal stability analysis of a helical vortex tube with axial flow. *J. Fluid Mech.* **738**, 222–249.

JIMÉNEZ, J., MOFFATT, H. K. & VASCO, C. 1996 The structure of the vortices in freely decaying two dimensional turbulence. *J. Fluid Mech.* **313**, 209–222.

KERSWELL, R. R. 2002 Elliptical instability. *Annu. Rev. Fluid Mech.* **34**, 83–113.

LACAZE, L., BIRBAUD, A.-L. & LE DIZÈS, S. 2005 Elliptic instability in a Rankine vortex with axial flow. *Phys. Fluids* **17**, 017101.

LACAZE, L., RYAN, K. & LE DIZÈS, S. 2007 Elliptic instability in a strained Batchelor vortex. *J. Fluid Mech.* **577**, 341–361.

LAPORTE, F. & CORJON, A. 2000 Direct numerical simulations of the elliptic instability of a vortex pair. *Phys. Fluids* **12** (5), 1016–1031.

LE DIZÈS, S. 2004 Viscous critical-layer analysis of vortex normal modes. *Stud. Appl. Maths* **112** (4), 315–332.

LE DIZÈS, S. & LACAZE, L. 2005 An asymptotic description of vortex Kelvin modes. *J. Fluid Mech.* **542**, 69–96.

LE DIZÈS, S. & LAPORTE, F. 2002 Theoretical predictions for the elliptic instability in a two-vortex flow. *J. Fluid Mech.* **471**, 169–201.

LEWEKE, T., LE DIZÈS, S. & WILLIAMSON, C. H. K. 2016 Dynamics and instabilities of vortex pairs. *Annu. Rev. Fluid Mech.* **48**, 507–541.

LEWEKE, T., QUARANTA, H. U., BOLNOT, H., BLANCO-RODRIGUEZ, F. J. & LE DIZÈS, S. 2014 Long- and short-wave instabilities in helical vortices. *J. Phys.: Conf. Ser.* **524**, 012154.

LEWEKE, T. & WILLIAMSON, C. H. K. 1998 Cooperative elliptic instability of a vortex pair. *J. Fluid Mech.* **360**, 85–119.

MAYER, E. W. & POWELL, K. G. 1992 Viscous and inviscid instabilities of a trailing vortex. *J. Fluid Mech.* **245**, 91–114.

MEUNIER, P. & LEWEKE, T. 2005 Elliptic instability of a co-rotating vortex pair. *J. Fluid Mech.* **533**, 125–159.

MOFFATT, H. K., KIDA, S. & OHKITANI, K. 1994 Stretched vortices – the sinews of turbulence; large-Reynolds-number asymptotics. *J. Fluid Mech.* **259**, 241–264.

MOORE, D. W. & SAFFMAN, P. G. 1975 The instability of a straight vortex filament in a strain field. *Proc. R. Soc. Lond.* A **346**, 413–425.

OKULOV, V. L. 2004 On the stability of multiple helical vortices. *J. Fluid Mech.* **521**, 319–342.

QUARANTA, H. U., BOLNOT, H. & LEWEKE, T. 2015 Long-wave instability of a helical vortex. *J. Fluid Mech.* **780**, 687–716.

ROY, C., SCHAEFFER, N., LE DIZÈS, S. & THOMPSON, M. 2008 Stability of a pair of co-rotating vortices with axial flow. *Phys. Fluids* **20**, 094101.

SIPP, D. & JACQUIN, L. 2003 Widnall instabilities in vortex pairs. *Phys. Fluids* **15**, 1861–1874.

TING, L. & TUNG, C. 1965 Motion and decay of a vortex in a nonuniform stream. *Phys. Fluids* **8** (6), 1039–1051.

TSAI, C.-Y. & WIDNALL, S. E. 1976 The stability of short waves on a straight vortex filament in a weak externally imposed strain field. *J. Fluid Mech.* **73** (4), 721–733.

WIDNALL, S. E. 1972 The stability of a helical vortex filament. *J. Fluid Mech.* **54**, 641–663.

WIDNALL, S. E., BLISS, D. & TSAI, C.-Y. 1974 The instability of short waves on a vortex ring. *J. Fluid Mech.* **66** (1), 35–47.

WIDNALL, S. E. & TSAI, C.-Y. 1977 The instability of the thin vortex ring of constant vorticity. *Phil. Trans. R. Soc. Lond.* A **287**, 273–305.

https://doi.org/10.1017/jfm.2016.533 Published online by Cambridge University Press